Journal of Computational Physics 450 (2022) 110815

Contents lists available at ScienceDirect

Journal of Computational Physics

www.elsevier.com/locate/jcp

A general computational framework for the dynamics of single- and multi-phase vesicles and membranes

Tiankui Zhang [a], Charles W. Wolgemuth [a,b,c,*]

[a] Department of Physics, University of Arizona, Tucson, AZ 85721, United States of America
[b] Department of Molecular and Cellular Biology, University of Arizona, Tucson, AZ 85721, United States of America
[c] Johns Hopkins Physical Sciences-Onocology Center, Johns Hopkins University, Baltimore, MD 21218, United States of America

ARTICLE INFO

Article history:
Available online 8 November 2021

Keywords:
Membrane dynamics
Endocytosis
Exocytosis
Biphasic vesicles

ABSTRACT

The dynamics of thin, membrane-like structures are ubiquitous in nature. They play especially important roles in cell biology. Cell membranes separate the inside of a cell from the outside, and vesicles compartmentalize proteins into functional microregions, such as the lysosome. Proteins and/or lipid molecules also aggregate and deform membranes to carry out cellular functions. For example, some viral particles can induce the membrane to invaginate and form an endocytic vesicle that pulls the virus into the cell. While the physics of membranes has been extensively studied since the pioneering work of Helfrich in the 1970's, simulating the dynamics of large scale deformations remains challenging, especially for cases where the membrane composition is spatially heterogeneous. Here, we develop a general computational framework to simulate the overdamped dynamics of membranes and vesicles. We start by considering a membrane with an energy that is a generalized functional of the shape invariants and also includes line discontinuities that arise due to phase boundaries. Using this energy, we derive the internal restoring forces and construct a level set-based algorithm that can stably simulate the large-scale dynamics of these generalized membranes, including scenarios that lead to membrane fission. This method is applied to solve for shapes of single-phase vesicles using a range of reduced volumes, reduced area differences, and preferred curvatures. Our results match well the experimentally measured shapes of corresponding vesicles. The method is then applied to explore the dynamics of multiphase vesicles, predicting equilibrium shapes and conditions that lead to fission near phase boundaries.

1. Introduction

One of the most important structures in biology is the lipid bilayer, a thin membranous structure that can be used to isolate cellular components into functional compartments like vesicles, endosomes, lysosomes, and the nucleus [1]. The plasma membrane even encloses the cell itself, defining what is the cell from what is not [2]. These membranes are composed of a variety of lipids and also surround and hold onto a range of different transmembrane and membrane-bound proteins [3]. The membrane is effectively a two-dimensional liquid crystal that flows under shear, bends elastically, and is mostly inextensible [4].

* Corresponding author.
E-mail address: wolg@email.arizona.edu (C.W. Wolgemuth).

https://doi.org/10.1016/j.jcp.2021.110815
0021-9991/

Unilamellar liposomes (also know as vesicles) are important model systems for cell membranes. Vesicles have been used to study membrane bending deformations [5], lipid phase separation and phase coexistence [6], protein interaction with biomembranes [7] and other physical processes on a cellular or subcellular level. These studies not only help us to better understand the biological membranes of living cells, but also provide insights into creating innovative drug delivery systems for treating cancer and other human diseases [8].

Much of the previous work focuses on homogeneous bilayers, often with symmetric shapes. It remains challenging to accurately simulate general lipid bilayer dynamics, which can include lateral inhomogeneity in lipid composition, protein interaction, and topological shape changes. One reason lies in the fact that bending forces for soft surfaces involve up to fourth order derivatives of the surface position, which can be difficult to compute convergently [9]. In addition, lipid bilayers can pinch off and fuse in important cellular events such as endocytosis, viral entry into and exit from cells, and nerve signal transduction [10–13]. Topological changes during these processes present difficulties in numerical simulation due to the presence of singularities. Moreover, membrane functions usually depend on the formation of local regions called lipid rafts [14], which maintain spatially-distinct chemical compositions and physical properties. A general physical understanding and mathematical description of the mesoscale dynamics of membrane geometry, especially including spatially-inhomogeneous regions, is still lacking.

In this paper, we address some of the theoretical and numerical problems mentioned above. In particular, we calculate generalized bending forces for a membrane whose energy is defined by an arbitrary functional that includes locally variable bending moduli and line forces that arise due to phase boundaries. These forces are derived using covariant differential geometry, so that the resulting forces are exact in the sharp interface limit and independent of the algorithmic framework that they are implemented in. We then develop a level-set approach to solve for the vesicle shape dynamics and phase boundary location. Partial differential equations governing those dynamics are presented, and a stable and relatively efficient numerical algorithm to handle these equations is developed. Numerical experiments are conducted and compared to experimental observations. Even though there have been numerous studies in this area, our development is unique in several aspects. First, the vesicle membrane is assumed to be nonuniform and the resulting bending forces can have nontrivial tangential components. Second, a general Hamiltonian for phase boundary line energies is proposed, and the variation of this Hamiltonian with respect to position is calculated. Third, we adopt the highly accurate numerical scheme developed in [15] to maintain second order accuracy of the bending forces in our simulations. Fourth, an adaptive semi-implicit scheme for the dynamical equations is presented. We make no assumptions on symmetry of the system and our simulations are carried out in fully three dimensional space.

This paper is organized as follows. We begin with an description of the dynamics and energetics of membranes. We then provide a brief, introduction to differential geometry, which is then used to formulate the mathematical description of a generalized Helfrich energy functional for vesicles with protein and lipid inhomogeneity. Variations of this energy lead to the force per unit area for these types of vesicles. Next, we describe our numerical discretization of geometrical quantities, which we use to develop a numerical scheme to handle the time-dependent PDEs for the overdamped dynamics of these systems. Finally, numerical results are presented and compared with previous experimental measurements.

2. The overdamped dynamics of vesicles

Unilamellar vesicles are isolated, fluid-filled regions enclosed by a lipid bilayer. The bilayer, itself, is thin, with a thickness of $\sim$5 nm [16], while the vesicle is typically substantially larger, being up to several microns in diameter [17]. Because the bilayer thickness is negligibly small compared to its extent, the bilayer can be treated as a two-dimensional surface embedded in the three-dimensional environment. Local motion of the bilayer membrane is impeded by the surrounding fluid. Since vesicles are at most microns in size with velocities on the order of microns per second, the Reynold's number, which is the ratio of fluid inertia to viscous forces, is on order of 10^{-3} or smaller. Therefore, the system is at low Reynold's number where viscous forces dominate and inertia is negligible [18]. The sum of the forces that act on any given point of the membrane is then approximately zero.

In this paper, we assume that there are two sources for the forces that act on the membrane, resistive forces from the fluid, $\boldsymbol{f}_r$, and forces arising from the configuration of the molecules that comprise the membrane, denoted as $\boldsymbol{f}$, that can be described by an energy functional (or Hamiltonian), $\mathcal{H}$. At low Reynold's number,

$$\boldsymbol{f} + \boldsymbol{f}_r = 0\,. \tag{1}$$

In general, the resistive force that acts on the membrane at position $\mathbf{x}$ is a non-local linear function of the fluid velocity field, $\mathbf{v}$ [18,19]:

$$\boldsymbol{f}_r(\mathbf{x}) = \iiint K(\mathbf{x},\mathbf{x}')\mathbf{v}(\mathbf{x}')\mathrm{d}^3\mathbf{x}'\,. \tag{2}$$

The kernel, $K(\mathbf{x},\mathbf{x}')$, depends on the specific shape of the membrane and the velocity field and can be determined by solving Stokes' equations. One method for computing the forces is through a Green's function approach, such as the Boundary Integral Method (BIM) [19]. However, for simplicity, we assume that the kernel is sharply peaked when $\mathbf{x}-\mathbf{x}'\approx 0$, which leads to a local resistive force, $\boldsymbol{f}_r \approx -\zeta\mathbf{v}$, where ζ is a drag coefficient. Consequently,

$$\zeta \mathbf{v} \approx \boldsymbol{f} \,, \tag{3}$$

defines the dynamics of the membrane. Note that only velocities that are perpendicular to the membrane affect the shape of the membrane, while velocities that are tangential to the membrane describe the flow of molecules along the surface. In principle, we expect that the drag coefficient ζ is not a single scalar, but rather that the motion normal to the surface has a different drag coefficient than motions tangential to the surface.

Given an energy functional, the force is determined from the change in the energy when the position of the membrane is varied. If the vector $\boldsymbol{R}$ describes the position of a material point on the membrane, then the energy $\mathcal{H} \to \mathcal{H} + \delta\mathcal{H}$ when the position is varied from $\boldsymbol{R} \to \boldsymbol{R} + \delta\boldsymbol{R}$, and the force is given by

$$\boldsymbol{f} = -\frac{\delta \mathcal{H}}{\delta \boldsymbol{R}} \approx \zeta \mathbf{v} \,, \tag{4}$$

where we have used Eq. (3) to relate the resistive force to the functional derivative of the energy.

3. Generalized membrane Hamiltonians and the differential geometry of surfaces

3.1. Hamiltonians for soft, fluidic, elastic surfaces

As written, Eq. (4) is a general statement of overdamped dynamics for the membrane. In order to solve for a specific case, the Hamiltonian needs to be defined. This Hamiltonian serves the same role as a constitutive law in elasticity theory [20]. In the 1970s, Helfrich proposed an elegant geometric model for lipid bilayers and successfully explained the biconcave shape of red blood cells [21]. His primary assumption was that the elastic energy density of a lipid bilayer is proportional to the square of the mean curvature of the membrane surface. This assumption is somewhat surprising, since at length scales on order of the size of lipid molecules, we expect that lipid fluidity, lipid stretching, lipid tilt and bilayer coupling all contribute to this energy. However, due to symmetry requirements, on scales large compared to the size of the lipid molecules, the forms of the Hamiltonian are limited and should only depend on geometric surface scalars, which for a surface are the mean and Gaussian curvatures, K_M and K, respectively. A natural expansion for this energy, as proposed in [22], is then

$$\begin{aligned}\mathcal{H} = \int \mathrm{d}A \Big\{ & C^{(0)} + C^{(1)} K_M + C^{(2,1)} K_M^2 + C^{(2,2)} K + C^{(3,1)} K_M^3 \\ & + C^{(3,2)} K_M K + C^{(4,1)} K_M^4 + C^{(4,2)} K_M^2 K + C^{(4,3)} K^2 \\ & + C^{(4,4)} (\nabla_\alpha K_M)(\nabla^\alpha K_M) + \mathcal{O}(\text{length}^{-5}) \Big\} \,.\end{aligned} \tag{5}$$

Usually only terms up to $\mathcal{O}(\text{length}^{-2})$ are adopted, although some research suggests that higher order terms may play a role in stability [23]. For inhomogenous bilayers, the phenomenological coefficients will vary spatially, depending on local concentrations of proteins and the specific lipid species present.

For lipid bilayers with open edges and/or phase coexistence, sharp discontinuities in material parameters can exist, leading to line energies that cannot be neglected. Based on similar symmetry arguments, a natural expansion for a general line energy depends on geometric invariants of the line, e.g., the geodesic curvature k_g, the normal curvature k_n, and the geodesic torsion τ_g. The line energy can then be written as

$$\mathcal{H} = \int \mathrm{d}l \{ c^{(0)} + c^{(1)} k_g + c^{(2)} k_n + c^{(3)} \tau_g + c^{(4)} B_\perp + c^{(5)} k_g^2 + c^{(6)} k_n^2 + \cdots \} \,, \tag{6}$$

where $B_\perp$ is the normal component of the curvature tensor (See Sec. 3.2). Line integrals, such as this, can be used to describe a variety of different interactions. For instance, the energy contribution due to open edges of nanodiscoids stabilized by edge-reactant salts can be written as $\mathcal{H} = \int_{\partial\mathcal{P}} \mathrm{d}l \{\tau + c_1 (k_g - k_0)^2 + c_2 k_n^2\}$ [24]. For membranes with phase boundaries, differences in Gaussian bending moduli lead to terms like $\mathcal{H} = \int \mathrm{d}l c^{(1)} k_g$ [25]. The specific form of Eqs. (5), (6) depends on the problem of interest.

In addition to these terms, a closed vesicle is also subject to a number of constraints. For example, the volume enclosed by the membrane, V_p, only changes if fluid can flow across the membrane. In addition, lipids do not readily flip from one leaflet of the bilayer to the other [26]. Therefore, to a good extent, each leaflet of the membrane is incompressible, which implies that the average surface area of the bilayer, A_p, and the difference in area between the leaflets, ΔA, are also fixed. These constraints can be imposed by adding them to the Hamiltonian using Lagrange multipliers. We follow the area-difference elasticity model [27], and add to our unconstrained Hamiltonian described above, which we denote as $\mathcal{H}_0$, integrals to enforce these three constraints:

$$\begin{aligned}\mathcal{H} = \mathcal{H}_0 & + \sigma \left(\int \mathrm{d}A - A_p \right) - P \left(\int \frac{\boldsymbol{R} \cdot \boldsymbol{N}}{3} \mathrm{d}A - V_p \right) \\ & + \sigma_{\Delta A} \left(h \int K_M \mathrm{d}A - \Delta A_p \right) \,,\end{aligned} \tag{7}$$

where the first and second integrals constrain the total area and total volume of the vesicle, respectively, and the last term constrains the area difference between the two layers. The Lagrange multipliers are σ, P, and $\sigma_{\Delta A}$, and h is the thickness of the bilayer. In Eq. (7) and all subsequent integrals, except where otherwise noted, the domain of integration consists of the entire surface area of the bilayer membrane.

When the vesicle deforms due to a velocity field $\boldsymbol{v}$, the time rate change of the total volume $V = \frac{1}{3}\int \boldsymbol{R}\cdot\boldsymbol{N}\mathrm{d}A$, total area $A = \int \mathrm{d}A$ and the area difference $\Delta A = h\int K_M \mathrm{d}A$ are

$$\frac{\mathrm{d}V}{\mathrm{d}t} = \int \boldsymbol{v}\cdot\boldsymbol{N}\mathrm{d}A\,, \tag{8}$$

$$\frac{\mathrm{d}A}{\mathrm{d}t} = \int (-K_M)(\boldsymbol{v}\cdot\boldsymbol{N})\mathrm{d}A\,, \tag{9}$$

$$\frac{\mathrm{d}(\Delta A)}{\mathrm{d}t} = h\int (-2K)(\boldsymbol{v}\cdot\boldsymbol{N})\mathrm{d}A\,. \tag{10}$$

Because Eqs. (8)-(10) relate the change in volume, area, and area difference to an integral of a function of the normal component of the velocity, these equations can be used as a system of linear equations for defining the Lagrange multiplers: $\sigma, P, \sigma_{\Delta A}$. By specifying the time rate of change for V, A, and/or ΔA, it is straightforward to solve for the Lagrange multipliers that preserve volume, area, and/or the area difference. These same equations can also be used to evolve those parameters in a prescribed manner [28]. It is often convenient to work in terms of a dimensionless volume and area difference defined by

$$v = \frac{V}{\frac{4}{3}\pi R_s^3}\,,\quad \Delta a = \frac{\Delta A}{8\pi h R_s}\,,\quad R_s = \sqrt{\frac{A}{4\pi}}\,, \tag{11}$$

where v is the *reduced volume*, Δa the *reduced area difference*, and $8\pi h R_s$ is the area difference of a spherical bilayer of radius R_s and thickness h.

3.2. Covariant description of surfaces and embedded lines

To find the internal restoring force for the membrane, we need to determine how the generalized Hamiltonian varies when the positions of material points on the membrane are varied. To do this calculation, we begin by computing the geometric invariants in terms of the position. These relationships are used to compute how the invariants change with variations in the membrane shape. The variation of the energy is then straightforward to determine. In this section we describe briefly the differential geometry of surfaces in a covariant manner, and use this description to define the shape invariants for surfaces and embedded lines.

The location of points on an effectively two-dimensional membrane can be described by a vector $\boldsymbol{R}$ that is parameterized by two local surface coordinates, $S^\alpha, \alpha \in \{1,2\}$. Because the membrane resides in three-dimensional space, the surface can also be parameterized using the subset of the 3D ambient space coordinates $Z^i(S^1, S^2)$, where $i \in \{1,2,3\}$ [29]. Note that Z^i can be arbitrary curvilinear coordinates. The position of a point Z in the ambient space is denoted by $\boldsymbol{R}(Z)$, which is an invariant physical quantity. The coordinate vectors of the ambient space are $\boldsymbol{Z}_i \equiv \partial\boldsymbol{R}/\partial Z^i$. We may also write the surface as $\boldsymbol{R}(S) = \boldsymbol{R}(Z(S))$, where we have ignored the indices for Z and S to simplify notation. By convention, superscripts are contravariant and subscripts are covariant. Latin letters i, j, k denote indices for the ambient space, while Greek letters α, β, γ denote indices for the surface. Einstein summation convention is assumed in this paper.

All of the geometrical information for the surface is encoded in the mapping $\boldsymbol{R}(S)$. The surface coordinate vectors that define the local tangent plane are

$$\boldsymbol{S}_\alpha \equiv \frac{\partial\boldsymbol{R}}{\partial S^\alpha} = \frac{\partial Z^i}{\partial S^\alpha}\frac{\partial\boldsymbol{R}}{\partial Z^i} = Z^i_\alpha \boldsymbol{Z}_i\,,$$

where Z^i_α are called *shift tensors*, since they shift the coordinate vectors in ambient space to the tangent space of the surface. The *metric tensor* is $S_{\alpha\beta} \equiv \boldsymbol{S}_\alpha\cdot\boldsymbol{S}_\beta$, which has determinant $S = e^{\alpha\beta}e^{\mu\nu}S_{\alpha\mu}S_{\beta\nu}/2!$, where $e^{\alpha\beta}$ is the permutation symbol. The unit normal of the surface is $\boldsymbol{N} = \boldsymbol{S}_1\times\boldsymbol{S}_2/|\boldsymbol{S}_1\times\boldsymbol{S}_2|$. In Fig. 1, $\{\boldsymbol{S}_1, \boldsymbol{S}_2, \boldsymbol{N}\}$ forms a right handed coordinate for the surface. The curvature of the surface is described by how the tangent vectors change as one moves along the surface. We can then define the *curvature tensor* as

$$B_{\alpha\beta} \equiv \boldsymbol{N}\cdot\nabla_\alpha\boldsymbol{S}_\beta = -\boldsymbol{S}_\beta\cdot\nabla_\alpha\boldsymbol{N} = \boldsymbol{N}\cdot\partial_\alpha\partial_\beta\boldsymbol{R}\,, \tag{12}$$

where ∇_α are covariant derivatives. The only two scalar invariants of the curvature tensor are its trace, $\mathrm{tr}(B) = K_M$ (the *mean curvature*), and the determinant, $\det(B) = K$ (the *Gaussian curvature*), which can also be written as

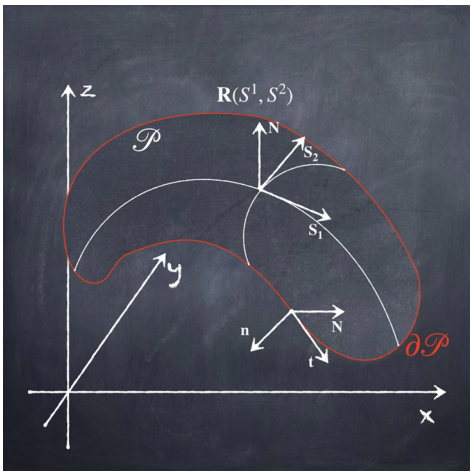

Fig. 1. A two dimensional surface patch $\mathcal{P}$ is defined by the vector $\boldsymbol{R}(Z(S))$, which describes the location of points on the membrane surface in the three dimensional ambient space. At any point on the membrane surface, a right-handed coordinate system can be defined $\{\mathbf{S}_1, \mathbf{S}_2, \mathbf{N}\}$, where $\mathbf{N}$ is the normal to the surface, and $\mathbf{S}_1$ and $\mathbf{S}_2$ lie along the tangents to the surface that follow the two local membrane coordinate directions, S^1 and S^2, respectively. Curves that live on the surface, such as the domain boundary $\partial\mathcal{P}$, are parameterized by a single arclength coordinate and have their own orthonormal triad $\{\mathbf{t}, \mathbf{n}, \mathbf{N}\}$, where $\mathbf{t}$ is the tangent to the curve, and $\mathbf{n}$ is normal to the curve in the plane of the membrane.

$$K_M \equiv \mathrm{tr}(B) = B^\alpha_\alpha = S^{\alpha\beta} B_{\alpha\beta} \,, \tag{13}$$

$$K \equiv \det(B) = \frac{1}{2!}\delta^{\alpha\beta}_{\mu\nu} B^\mu_\alpha B^\nu_\beta = \frac{1}{2}\varepsilon^{\alpha\beta}\varepsilon^{\mu\nu} B_{\alpha\mu} B_{\beta\nu} \,, \tag{14}$$

where $S^{\alpha\beta}$ is the inverse of $S_{\alpha\beta}$, $\delta^{\alpha\beta}_{\mu\nu}$ is the Kronecker delta and $\varepsilon^{\alpha\beta}$ is the Levi-Civita tensor defined as $\varepsilon_{\alpha\beta} = \sqrt{S} e_{\alpha\beta}, \varepsilon^{a\beta} = e^{\alpha\beta}/\sqrt{S}$. In this convention, the mean curvature of the unit sphere is -2.

The boundary of an open patch of surface $\mathcal{P}$, denoted by $\partial\mathcal{P}$, is an embedded curve on the surface. Mathematically, this curve can be represented as a mapping from $\mathbb{R}$ to $\mathbb{R}^3$ through composition of $S(U) : U^\Phi \to S^\alpha$ and $Z(S) : S^\alpha \to Z^i$, where U^Φ is the contravariant curve coordinate, and $\Phi = 1$. We use capital Greek letters Φ, Ψ to denote curve indices. The curve can also be written as $\boldsymbol{R}(U) = \boldsymbol{R}(Z(S(U)))$. Similarly, we may define the curve coordinate vector as $\boldsymbol{U}_\Phi = \partial \boldsymbol{R}/\partial U^\Phi$. The corresponding *metric tensor* is $U_{\Phi\Psi} = \boldsymbol{U}_\Phi \cdot \boldsymbol{U}_\Psi$. The determinant of $U_{\Phi\Psi}$ is $U = e^\Phi e^\Psi U_{\Phi\Psi}$ where e^Φ is the one-dimensional permutation symbol and is always equal to one. The Levi-Civita tensor in this one-dimensional curve is $\varepsilon_\Phi = \sqrt{U} e_\Phi, \varepsilon^\Phi = e^\Phi/\sqrt{U}$. The unit tangent of the curve is

$$\boldsymbol{t} = \varepsilon^\Phi \boldsymbol{U}_\Phi = \varepsilon^\Phi \nabla_\Phi \boldsymbol{R} = \nabla_s \boldsymbol{R} \,, \tag{15}$$

where ∇_Φ is the covariant derivative and $\nabla_s \equiv \varepsilon^\Phi \nabla_\Phi$ is an invariant derivative. The coordinate vector can also be written as $\boldsymbol{U}_\Phi = \varepsilon_\Phi \boldsymbol{t}$. Since the curve tangent $\boldsymbol{t}$ lives in the tangential space of the surface, we can decompose $\boldsymbol{t}$ as $\boldsymbol{t} = t^\alpha \boldsymbol{S}_\alpha$. The unit normal $\boldsymbol{n}$ of the curve within the surface is $\boldsymbol{n} = n^\alpha \boldsymbol{S}_\alpha = \varepsilon^{\alpha\beta} t_\beta \boldsymbol{S}_\alpha$. Along $\partial\mathcal{P}$, $\{\boldsymbol{t}, \boldsymbol{N}, \boldsymbol{n}\}$ forms an orthonormal coordinate system known as the *Darboux frame*, which can be decomposed in the Z coordinates as $\boldsymbol{t} = t^i \boldsymbol{Z}_i, \boldsymbol{N} = N^i \boldsymbol{Z}_i, \boldsymbol{n} = n^i \boldsymbol{Z}_i$ and conversely, $\boldsymbol{Z}_i = t_i \boldsymbol{t} + N_i \boldsymbol{N} + n_i \boldsymbol{n}$. Rates of change of the Darboux frame as one moves along the curve define the curvature of the curve. In fact,

$$\nabla_s \boldsymbol{t} = k_g \boldsymbol{n} + k_n \boldsymbol{N} \,, \tag{16}$$

$$\nabla_s \boldsymbol{n} = -k_g \boldsymbol{t} + \tau_g \boldsymbol{N} \,, \tag{17}$$

$$\nabla_s \boldsymbol{N} = -k_n \boldsymbol{t} - \tau_g \boldsymbol{n} \,, \tag{18}$$

$$\nabla_\perp \boldsymbol{N} = -\tau_g \boldsymbol{t} - B_\perp \boldsymbol{n} \,, \tag{19}$$

where $\nabla_\perp \equiv \boldsymbol{n} \cdot \nabla$ is the direction derivative along the $\boldsymbol{n}$ direction, and we have defined the *geodesic curvature* $k_g \equiv n_\alpha \nabla_s t^\alpha$, the *normal curvature* $k_n \equiv t^\alpha t^\beta B_{\alpha\beta}$, the geodesic torsion $\tau_g \equiv n^\alpha t^\beta B_{\alpha\beta}$, and $B_\perp \equiv n^\alpha n^\beta B_{\alpha\beta}$. In this convention, smaller circles of radius $r < 1$ on a unit sphere have geodesic curvature $k_g = -\sqrt{1-r^2}/r$. Obviously, $\begin{pmatrix} k_n & \tau_g \\ \tau_g & B_\perp \end{pmatrix}$ represents the curvature tensor $B_{\alpha\beta}$ in the Darboux frame. Since curvature scalars are invariant along the curve, we have

$$K_M = k_n + B_\perp \,,$$
$$K = k_n B_\perp - \tau_g^2 \,.$$

3.3. Forces arising from variations in a generalized Helfrich Hamiltonian

The variation of the Helfrich bending energy was first carried out by Ou-Yang [30], and the process was made more elegant using covariant notation by Capovilla and Guven [31]. In these works and others, the vesicles are usually assumed to be homogeneous with constant phenomenological coefficients. Thus, the resulting bending forces from a generalized Helfrich-type Hamiltonian, i.e., Eq. (5), is still lacking. In order to handle this broader class of problems, we assume that all the phenomenological coefficients in Eq. (5) vary locally on the surface and derive a fully general description of the membrane bending force.

Since the general energy functional is an integral over the surface area of terms involving the mean and Gaussian curvatures, precomputing these variations simplifies the computation of the variation of the energy. We denote the variation of the position by $\boldsymbol{R}(S) \to \boldsymbol{R}(S) + \delta\boldsymbol{R}(S)$, and decompose $\delta\boldsymbol{R}$ into its tangential and normal components, $\delta\boldsymbol{R} = \boldsymbol{W}(S) = W\boldsymbol{N} + W^\alpha \boldsymbol{S}_\alpha$. We then use this expression to compute the variation of the tangent and normal vectors:

$$\begin{aligned}
\delta\boldsymbol{S}_\alpha &= \delta(\nabla_\alpha \boldsymbol{R}) \\
&= \nabla_\alpha(\delta\boldsymbol{R}) \\
&= (\nabla_\alpha W + W^\beta B_{\alpha\beta})\boldsymbol{N} + (\nabla_\alpha W^\beta - W B_\alpha^\beta)\boldsymbol{S}_\beta \,, \qquad (20)\\
\delta\boldsymbol{N} &= \delta\boldsymbol{N}\cdot(\boldsymbol{S}_\alpha \otimes \boldsymbol{S}^\alpha + \boldsymbol{N}\otimes\boldsymbol{N}) \\
&= -(\boldsymbol{N}\cdot\delta\boldsymbol{S}_\alpha)\boldsymbol{S}^\alpha \\
&= -(\nabla_\alpha W + W^\beta B_{\alpha\beta})\boldsymbol{S}^\alpha \,. \qquad (21)
\end{aligned}$$

From these, it is straightforward to compute the variations of the surface area differential $\mathrm{d}A$,

$$\delta(\mathrm{d}A) = \delta\left(\sqrt{S}\mathrm{d}S^1\mathrm{d}S^2\right) = (\nabla_\alpha W^\alpha - W K_M)\mathrm{d}A \,, \qquad (22)$$

and the variations of the mean and Gaussian curvatures,

$$\delta K_M = W(K_M^2 - 2K) + \Delta W + W^\nu \nabla_\nu K_M \,, \qquad (23)$$

$$\delta K = K K_M W + K_M \Delta W - B^{\alpha\beta}\nabla_\alpha\nabla_\beta W + W^\alpha \nabla_\alpha K \,, \qquad (24)$$

where $\Delta \equiv \nabla^\alpha\nabla_\alpha$ is the Laplace Beltrami operator. Variations of the metric tensors, metric determinant, and curvature tensor are given in Appendix A.

We are now ready to compute the variation of the energy. For an energy functional of the general form $\int_{\mathcal{P}} f\mathrm{d}A$, the variation is given by

$$\begin{aligned}
\delta\int_{\mathcal{P}} f\mathrm{d}A &= \int_{\mathcal{P}}\left(\delta f + f\frac{\delta(\mathrm{d}A)}{\mathrm{d}A}\right)\mathrm{d}A \\
&= \int_{\mathcal{P}}\{\delta f + f(\nabla_\alpha W^\alpha - W K_M)\}\mathrm{d}A \\
&= \int_{\mathcal{P}}(\delta f - \nabla_\alpha f W^\alpha - f K_M W)\mathrm{d}A + \int_{\mathcal{P}}\nabla_\alpha(f W^\alpha)\mathrm{d}A \qquad (25)\\
&= \int_{\mathcal{P}}(\delta f - \nabla_\alpha f W^\alpha - f K_M W)\mathrm{d}A + \int_{\partial\mathcal{P}} n_\alpha f W^\alpha \mathrm{d}l \\
&= \int_{\mathcal{P}}\delta\boldsymbol{R}\cdot\left(\frac{\delta f}{\delta\boldsymbol{R}} - \nabla_\parallel f - f K_M \boldsymbol{N}\right)\mathrm{d}A + \int_{\partial\mathcal{P}}\delta\boldsymbol{R}\cdot(f\boldsymbol{n})\mathrm{d}l \,,
\end{aligned}$$

where in the last step we used Stokes' law to convert a surface integral into a line integral and $\nabla_\parallel \equiv \boldsymbol{S}^\alpha\nabla_\alpha$ is the gradient operator on the surface. Thus, the force per area that arises from the energy density f is

$$\boldsymbol{f} = -\frac{\delta f}{\delta\boldsymbol{R}} + \nabla_\parallel f + f K_M \boldsymbol{N} \,, \qquad (26)$$

and the force per length at the boundary of the surface patch is

$$\boldsymbol{g}|_{\partial\mathcal{P}} = -f\boldsymbol{n} \,. \qquad (27)$$

When f does not depend on the geometry of the surface, $\delta f = 0$, and Eq. (26) reduces to

$$\boldsymbol{f} = \nabla_{\parallel} f + f K_M \boldsymbol{N} \,. \tag{28}$$

With Eq. (26) and Eqs. (20)-(24), it is straightforward to compute variations of the Hamiltonian (Eq. (5)) and the corresponding elastic forces.

In Appendix B, we use Eq. (28) to compute the forces for a set of representative energy terms that define all possible variations of the curvature Hamiltonian Eq. (5). One thing to note is that we use $\delta\kappa = 0$ in these calculations, which assumes that κ depends only on the surface coordinates (S^1, S^2). This assumption treats κ as a material property of the membrane that doesn't change when the 3D position of the surface is varied. Thus, κ is a field that simply moves along with the surface, behaving like a color field. We shall show that when κ depends on concentrations of lipids and/or proteins, $\delta\kappa$ is no longer zero, which will lead to extra forces that are important in describing the protein/lipid membrane interaction.

Now we turn to the variation of the line energy Eq. (6). The variation of the first two terms of Eq. (6) have been obtained previously by Capovilla [32] and then by Tu [33] via the method of differential forms. In this section, we calculate the variation of all possible terms in Eqs. (5)-(6) in a covariant form.

The variation of the position of the curve is just $\delta\boldsymbol{R}$ restricted to the curve, which can be written as $\delta\boldsymbol{R} = \boldsymbol{W}(U) = W\boldsymbol{N} + W^{\alpha}\boldsymbol{S}_{\alpha} = W^{i}\boldsymbol{Z}_{i}$, where W^{i} are components of $\boldsymbol{W}$ in the $\boldsymbol{Z}_i$ direction. Since $\boldsymbol{W}(U)$ is restricted to the curve, $\nabla_{\perp}\boldsymbol{W} = 0$. The variation of the tangent vector is

$$\delta\boldsymbol{U}_{\Phi} = \delta(\nabla_{\Phi}\boldsymbol{R}) = \nabla_{\Phi}\boldsymbol{W} = \varepsilon_{\Phi}\nabla_s\boldsymbol{W} \,, \tag{29}$$

and, therefore, the variation of the unit tangent is

$$\delta\boldsymbol{t} = \delta(\varepsilon^{\Phi}\boldsymbol{U}_{\Phi}) = (\mathbb{1} - \boldsymbol{t}\otimes\boldsymbol{t})\cdot\nabla_s\boldsymbol{W} = (\boldsymbol{n}\otimes\boldsymbol{n} + \boldsymbol{N}\otimes\boldsymbol{N})\cdot\nabla_s\boldsymbol{W} \,,$$

where we used the decomposition of the identity operator $\mathbb{1}$ in the Darboux frame: $\mathbb{1} = \boldsymbol{t}\otimes\boldsymbol{t} + \boldsymbol{n}\otimes\boldsymbol{n} + \boldsymbol{N}\otimes\boldsymbol{N}$. The variations of the metrics for the curve are given in Appendix A. Note also that the variations of the surface geometric terms along the curve, such as those for $\boldsymbol{S}_{\alpha}, \boldsymbol{N}, K_M$, are still given by Eqs. (20)-(24) with the restriction that $\nabla_{\perp}\boldsymbol{W} = 0$.

The variation of the length differential $\mathrm{d}l$ is

$$\delta(\mathrm{d}l) = \delta\left(\sqrt{U}\mathrm{d}U^1\right) = (\boldsymbol{t}\cdot\nabla_s\boldsymbol{W})\mathrm{d}l \,, \tag{30}$$

and for the curve normal $\boldsymbol{n}$ is

$$\delta\boldsymbol{n} = -(\boldsymbol{n}\cdot\delta\boldsymbol{t})\boldsymbol{t} - (\boldsymbol{n}\cdot\delta\boldsymbol{N})\boldsymbol{N} = -(\boldsymbol{n}\cdot\nabla_s\boldsymbol{W})\boldsymbol{t} + n^{\alpha}W^{\beta}B_{\alpha\beta}\boldsymbol{N} \,. \tag{31}$$

To compute the variation of k_g, k_n and τ_g, we first compute $\delta(\nabla_s\boldsymbol{t})$ and $\delta(\nabla_s\boldsymbol{N})$, which are straightforward to calculate:

$$\begin{aligned}
\delta(\nabla_s\boldsymbol{t}) &= \delta(\varepsilon^{\Phi}\nabla_{\Phi}\boldsymbol{t}) \\
&= \delta\varepsilon^{\Phi}\nabla_{\Phi}\boldsymbol{t} + \varepsilon^{\Phi}\nabla_{\Phi}(\delta\boldsymbol{t}) \\
&= -(\boldsymbol{t}\cdot\nabla_s\boldsymbol{W})\nabla_s\boldsymbol{t} + \nabla_s(\delta\boldsymbol{t}) \\
&= \nabla_s^2\boldsymbol{W} - (\nabla_s\boldsymbol{t}\cdot\nabla_s\boldsymbol{W})\boldsymbol{t} - (\boldsymbol{t}\cdot\nabla_s^2\boldsymbol{W})\boldsymbol{t} - 2(\boldsymbol{t}\cdot\nabla_s\boldsymbol{W})\nabla_s\boldsymbol{t} \,,
\end{aligned} \tag{32}$$

$$\begin{aligned}
\delta(\nabla_s\boldsymbol{N}) &= \delta(\varepsilon^{\Phi}\nabla_{\Phi}\boldsymbol{N}) \\
&= \delta\varepsilon^{\Phi}\nabla_{\Phi}\boldsymbol{N} + \varepsilon^{\Phi}\nabla_{\Phi}(\delta\boldsymbol{N}) \\
&= -(\boldsymbol{t}\cdot\nabla_s\boldsymbol{W})\nabla_s\boldsymbol{N} + \nabla_s(\delta\boldsymbol{N}) \\
&= -(\boldsymbol{t}\cdot\nabla_s\boldsymbol{W})\nabla_s\boldsymbol{N} - \nabla_s(t_{\alpha}\nabla_s W + W^{\beta}B_{\alpha\beta})\boldsymbol{S}^{\alpha} \\
&\quad -(k_n\nabla_s W + W^{\beta}t^{\gamma}B_{\alpha\beta}B^{\alpha}_{\gamma})\boldsymbol{N} \,.
\end{aligned} \tag{33}$$

The variations of the geodesic curvature k_g, the normal curvature k_n, and the geodesic torsion are then

$$\begin{aligned}
\delta k_g &= \delta(\boldsymbol{n}\cdot\nabla_s\boldsymbol{t}) \\
&= \boldsymbol{n}\cdot\delta(\nabla_s\boldsymbol{t}) + \delta\boldsymbol{n}\cdot\nabla_s\boldsymbol{t} \\
&= \boldsymbol{n}\cdot\nabla_s^2\boldsymbol{W} - 2k_g(\boldsymbol{t}\cdot\nabla_s\boldsymbol{W}) + k_n n^{\alpha}W^{\beta}B_{\alpha\beta} \,,
\end{aligned} \tag{34}$$

$$\begin{aligned}
\delta k_n &= \delta(\boldsymbol{N}\cdot\nabla_s\boldsymbol{t}) \\
&= \boldsymbol{N}\cdot\delta(\nabla_s\boldsymbol{t}) + \delta\boldsymbol{N}\cdot\nabla_s\boldsymbol{t} \\
&= \boldsymbol{N}\cdot\nabla_s^2\boldsymbol{W} - 2k_n(\boldsymbol{t}\cdot\nabla_s\boldsymbol{W}) - k_g n^{\alpha}W^{\beta}B_{\alpha\beta} \,,
\end{aligned} \tag{35}$$

$$\begin{aligned}
\delta\tau_g &= -\delta(\boldsymbol{n}\cdot\nabla_s\boldsymbol{N}) \\
&= -\delta\boldsymbol{n}\cdot\nabla_s\boldsymbol{N} - \boldsymbol{n}\cdot\delta(\nabla_s\boldsymbol{N}) \\
&= -(k_n + \tau_g)(\boldsymbol{t}\cdot\nabla_s\boldsymbol{W}) + n^{\alpha}\nabla_s(t_{\alpha}\nabla_s W + W^{\beta}B_{\alpha\beta}) \,.
\end{aligned} \tag{36}$$

With these definitions, we can compute the variation of $\oint_{\partial\mathcal{P}} f\,\mathrm{d}l$,

$$\begin{aligned}\delta\oint_{\partial\mathcal{P}} f\,\mathrm{d}l &= \oint_{\partial\mathcal{P}}\left(\delta f + f\frac{\delta(\mathrm{d}l)}{\mathrm{d}l}\right)\mathrm{d}l\\ &= \oint_{\partial\mathcal{P}}(\delta f + f t^i \nabla_s W_i)\mathrm{d}l\\ &= \oint_{\partial\mathcal{P}}\{\delta f - \boldsymbol{W}\cdot\nabla_s(f\boldsymbol{t})\}\mathrm{d}l\,.\end{aligned} \tag{37}$$

The force per length along the curve is then

$$\boldsymbol{g}|_{\partial\mathcal{P}} = -\frac{\delta f}{\delta \boldsymbol{R}} + \nabla_s(f\boldsymbol{t})\,. \tag{38}$$

In Appendix B, we use Eqs. (29)-(38) to compute the forces for the set of representative line energy terms that define all possible variations of the curvature Hamiltonian Eq. (6), thereby determining all possible forces that arise from a Hamiltonian consisting of line curvature scalars. While we will not explore the numerical impacts of all terms in the Hamiltonian (Eqs. (5) and (6)), these calculations enable the development of membrane models that go substantially beyond the canonical curvature squared model of Helfrich theory. In addition, they are decoupled from the numerical schemes presented in the next section and can be used in any applications that adopt a more general description of elastic bilayers.

4. Algorithms for vesicle dynamics driven by a general Hamiltonian

As shown in the previous section, a generalized Helfrich-type Hamiltonian $\mathcal{H}$ leads to two types of forces, spatially distributed forces per unit area and localized forces per unit length that act at membrane and phase boundaries. When constructing an algorithm to solve Eq. (4), we must be able to account for the three-dimensional motion of the two-dimensional membrane surface itself, while also tracking the movement of one dimensional boundaries that reside on the membrane surface. In addition, because we are interested in applying this method to biological situations that can involve membrane fission and fusion events, such as occur during endocytosis and exocytosis, we also need a method that can handle topological changes to the membrane.

Numerically, two dimensional surfaces can be represented explicitly as point clouds and triangular/quadrilateral surface patches or implicitly as the level set of a higher dimensional scalar function. The quality of an explicit surface representation usually depends heavily on the quality of the triangular/quadrilateral surface elements. Complicated meshing and remeshing methods [34] are then required to maintain accuracy of the numerical scheme when the surface undergoes large deformation. Recently, a survey of different methods to discretize bending forces showed that most algorithms based on a surface triangulation are not convergent in the computation of the Laplacian of the mean curvature, ΔK_M [9]. Since membrane bending forces involve this term and other terms involving second derivatives of the membrane curvatures, we are not aware of current methods from which to construct a convergent algorithm that uses an explicit surface representation.

When the surface is represented implicitly, as is the case with the level set method [35] and the phase field method [36], a scalar field (the level set function or the phase order parameter) on an Eulerian gird is used to track the position of the surface. With this implicit representation, geometrical quantities such as the curvature can be easily computed. Moreover, topological changes can be captured more elegantly, without sophisticated surgeries of an explicit surface mesh.

For these reasons, our numerical framework adopts the level set method introduced by Osher and Sethian [37], specifically utilizing the implementation described in [35]. The phase field method is also commonly used in the simulation of elastic surfaces [36,38]. However, there is one important limitation on this diffuse interface approach. In the phase field method, the interface is represented as a thin layer of thickness ϵ over which the order field ϕ changes most rapidly and the Helfrich energy density K_M^2 is approximated by $\frac{\epsilon}{2}\left|\Delta\phi - \frac{1}{\epsilon^2}(\phi^2-1)\phi\right|^2$ [36]. While this approximation converges to give the correct forces for the standard Helfrich energy [21], it is not known whether it will also converge appropriately for more generalized Hamiltonians (e.g., ones that include spatially variable parameters and sharp discontinuities). It is then unclear whether the phase field method will always provide an algorithm that converges to the correct forces, and therefore give the correct dynamics. However, we have shown that the Level Set Method can provide a convergent means for computing the geometric quantities that define the forces in these generalized Hamiltonians [15]. Also, although gradient descent, commonly used with the phase field method for both static [36] and dynamical simulations [38], can surely lead to a local energy minimum, the dynamics may not obey the correct physical forces. These limitations are avoided with the level set approach because physical forces driving evolution of the system are directly discretized on the sharp interface and new interactions can be readily accounted for.

In the level set method, the two-dimensional membrane shape is given by the zero level set of a signed distance function, ϕ, with the dynamics of this function given by

$$\frac{\partial \phi}{\partial t} + \boldsymbol{v} \cdot \nabla \phi = 0 \,. \tag{39}$$

This equation forms the backbone for our algorithm. Given a Hamiltonian and the current configuration of the membrane, the local velocity $\mathbf{v}$ can be determined from Eq. (4). However, the force $\boldsymbol{f}$ contains terms involving second derivatives of the curvature of the membrane, which are the same as fourth derivatives of ϕ. These high order derivatives in the definition of the velocity cause Eq. (39) to be very stiff, which then requires an exceedingly small time step when explicit methods are used. Therefore, we adopt the semi-implicit level set method from [39] to evolve Eq (39). With this semi-implicit approach, Eq. (39) is discretized in time as

$$\frac{\phi^{n+1} - \phi^n}{\Delta t} = \alpha\{(\Delta^2\phi)^n - (\Delta^2\phi)^{n+1}\} - (\boldsymbol{v} \cdot \nabla\phi)^n \,, \tag{40}$$

which can be rewritten as

$$\phi^{n+1} = \phi^n - \Delta t(\mathbb{1} + \alpha \Delta t \Delta^2)^{-1}(\boldsymbol{v} \cdot \nabla\phi)^n \,, \tag{41}$$

where α is a positive constant (taken to be 0.5 in our simulations) and Δ^2 is the biLaplacian. Using periodic boundary conditions set sufficiently far from the interface, an approximate inversion of $(\mathbb{1} + \alpha\Delta t\Delta^2)^{-1}$ can be computed efficiently with Fast Fourier Transform (FFT) methods. If necessary, a more accurate solution of Eq. (41) can be obtained using the FFT operator as a preconditioner in the GMRES (generalized minimal residual) method. While the GMRES solver gives slightly better stability and accuracy, solely using the FFT method is much more efficient computationally. Therefore, we use the FFT solver in the simulations presented here.

4.1. Algorithm for single phase vesicles

We begin by describing our algorithm for vesicles that do not have sharp discontinuities in the material parameters, such as occur at phase boundaries. For these cases, the forces derived from Eq. (4) are smoothly varying functions of position, and line tension-type forces are not present. In this case, we can describe the vesicle with a single signed distance map ϕ and evolve it using Eq. (41).

The algorithm to evolve the membrane shape is then as follows:

1. Initialize the level set function ϕ on a three dimensional cartesian grid. Usually ϕ is initialized to be an oblate or prolate ellipsoid with a prescribed reduced volume and then reinitialized to be a signed distance map. The ellipsoid is usually taken to be cylindrically symmetric, the reduced volume of which is then a function of the ratio between the lengths of the two distinct semi-axes.
2. Repeat the following until either a maximum time or maximum number of iterations is reached:
   i. Calculate K_M and K using the discretizations given in Sec. 4.3 at all grid points and extend their values away from the interface using the sixth order accurate extension scheme described in [15].
   ii. Calculate the Laplacian of the mean curvature in the tangent plane $\Delta_\parallel K_M$ (See Sec. 4.3) at all grid points and extend its value away from the interface. Note that because we extend K_M away from the surface such that the normal component of its gradient is zero, the standard 3D Cartesian Laplacian can be used in place of $\Delta_\parallel$ when computing $\Delta_\parallel K_M$.
   iii. Using the geometric terms from step ii, calculate the force $\boldsymbol{f}$ without the Lagrange multipliers σ, P, and $\sigma_{\Delta A}$, and calculate an intermediate value of the velocity $\boldsymbol{v}' = \boldsymbol{f}/\zeta$.
   iv. Find the maximum value of $|\boldsymbol{v}'|$, $v_{\max}$, near the interface and use $v_{\max}\Delta t = N_{\mathrm{CFL}}\Delta s$ to determine time step Δt, where N_{CFL} is the CFL number for the current step and Δs is the grid spacing in each dimension. The CFL number is taken to be 0.1 for the sake of stability and accuracy although larger values can also be used.
   v. Solve for the Lagrange multipliers by specifying $\mathrm{d}V/\mathrm{d}t$, $\mathrm{d}A/\mathrm{d}t$, and $\mathrm{d}(\Delta A)/\mathrm{d}t$ using Eqs. (8), (9), and (10).
   vi. Calculate the complete force $\boldsymbol{f}$ that includes the Lagrange multiplier terms, and use it to define $\boldsymbol{v}$ from Eq. (4). Extend the velocity away from the interface using the methods described in [15], which will maintain ϕ as a signed distance map [40].
   vii. Update ϕ with Eq. (41).
   viii. Reinitialize ϕ to be a signed distance function, if necessary. In order to maintain ϕ as a distance map, which helps maintain the accuracy and stability of the Level Set Method, we reinitialize ϕ every 10 iterations.

In order to maintain second-order accuracy of the bending forces, which scale like fourth derivatives of ϕ, the extension of quantities away from the interface and reinitialization of ϕ that occur in steps i, ii, vi and viii are handled with the sixth-order accurate method described in [15].

4.2. Algorithm for multiphase vesicles

In multiphase vesicles, phase boundaries exist in the membrane and evolve in time. The dynamics of these boundary curves need to be computed simultaneously with the motion of the membrane. Because we are using the level set method,

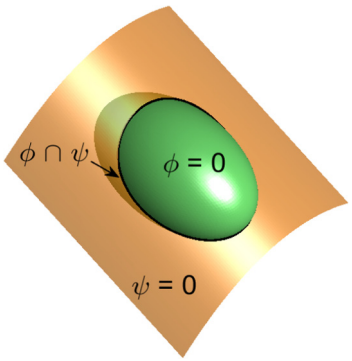

Fig. 2. An oblate vesicle is defined as the zero contour of the signed distance function ϕ (green). The zero contour of a second distance function ψ (copper) intersects the membrane along a closed curve (black line). (For interpretation of the colors in the figure(s), the reader is referred to the web version of this article.)

these situations are straightforward to handle. If the membrane is defined as the level set $\phi(\mathbf{x}) = 0$, a closed curve on the membrane can be given by the intersection of the zero contour of ϕ with the zero level set of a second signed distance function ψ, as shown in Fig. 2.

In [41], it was shown that to obtain a convergent scheme for calculating the length of phase boundaries, ϕ and ψ should be signed distance functions with their zero level sets orthogonal to each other. In our numerical experiments, we found that defining ψ as a signed geodesic distance function gives better stability. Because ψ is a level set function, its dynamics are also defined by Eq. (39) and can be time-stepped using Eq. (41). The velocity function that evolves ψ needs to satisfy two conditions. First, it has to accurately model the phase boundary motion in the plane of the membrane, and it also needs to maintain itself as a geodesic signed distance function. Therefore,

$$\frac{\partial \psi}{\partial t} + v_{\text{bo}}|\nabla\psi| = -\frac{\delta \mathcal{H}_{\text{reg}}}{\partial \psi}\,, \tag{42}$$

where v_{bo} is the dynamic velocity that describes the phase boundary motion in the plane of the membrane (details for how this is derived from the Hamiltonian are given in Sec. 5.2.1). The right hand side of this equation includes an additional energy term, $\mathcal{H}_{\text{reg}}$, that helps maintain ψ as a signed distance function with contours that are perpendicular to the surface, with

$$\mathcal{H}_{\text{reg}}(\psi, \nabla\psi) = \int \frac{D_N}{2}(\boldsymbol{N}\cdot\nabla\psi)^2 \mathrm{d}V + \int p(|\nabla\psi|)\mathrm{d}V\,. \tag{43}$$

The first integral in Eq. (43) spreads ψ diffusively in the normal direction of the surface, $\boldsymbol{N}$, with a diffusion coefficient D_N. This term has been used previously in phase-field methods [42] to keep the zero level sets of the two distance maps orthogonal. The second integral in Eq. (43) is adopted from the distance regularized level set method developed by Li [43,44], where $p(|\nabla\psi|)$ has a minimum value of zero at $|\nabla\psi| = 1$. Minimization of $\int p(|\nabla\psi|)\mathrm{d}V$ will help keep $|\nabla\psi|$ close to 1. This functional plays a similar role to the Lyapunov functional giving rise to the Cahn-Hilliard equation for phase separation. We set $p(|\nabla\psi|)$ to be a quadratic function following [43]

$$p(|\nabla\psi|) = \frac{D_n}{2}(1 - |\nabla\psi|)^2.$$

More choices of $p(|\nabla\psi|)$ are discussed in [44]. In practice, we only use the regularizing Hamiltonian in Eq. (43) when a narrow neck is detected in the phase boundaries. Otherwise, we use the geodesic reinitialiazation procedure described in [15] in place of defining this Hamiltonian. In the simulations described later, we use $D_N = D_n = 1$, as these values were determined to provide enough smoothing without noticeably altering the dynamics.

For multiphasic vesicles, the area of each phase must be constrained. When there are two phases, we can denote the surface area of one phase as A^+ and that for the other phase as A^-. In this case, there is an associated Lagrange multiplier for each of these constraints, σ^+ and σ^-, respectively.

With multiphase vesicles, we have also found it is sometimes necessary to explicitly enforce local incompressibility of the membrane. We handle this using a soft constraint by defining a scalar field c on the membrane that measures local compression or stretching. The dynamics of c are given by a continuity equation that drives the motion of c along the surface of the membrane:

$$\frac{\partial c}{\partial t} + \nabla_{\parallel}\cdot(c\boldsymbol{v}) = 0\,, \tag{44}$$

where $\boldsymbol{v}$ is the velocity field of the vesicle, and $\nabla_{\parallel}$ is the gradient along the two-dimensional surface of the membrane. Since the membrane is presumed to be locally incompressible, the motion of the membrane should preserve the local value of c.

Deviations of c from its initial value, then, signify stretching or compression. We set an initial value of $c = 1$ everywhere, and add a term to the Hamiltonian that applies forces to the membrane that drive $c \to 1$:

$$\mathcal{H}_c = \int \mathrm{d}A \frac{\mu}{2} \left[(1-c)^2 + \left(1 - \frac{1}{c}\right)^2 \right] . \tag{45}$$

The variable c is effectively the determinant of the metric tensor and is inversely related to the mass density of the surface. The first term in the integral gives a linear elastic response for changes in area, while the second term penalizes changes in the density. A large elastic moduli μ in Eq. (45) keeps the vesicle effectively incompressible by penalizing deviations of c from 1. This idea of defining a local field measuring local stretching is adopted from [45].

For multiphase vesicles, we then have three functions to evolve through time: ϕ, ψ, and c. The dynamics of all three of these function are handled with the same semi-implicit scheme as is for Eq. (39). For the lipid density field c, we use diffusion operator Δ to smooth its dynamics. For ψ, we still use the BiLaplacian operator. Thus, ϕ, c and ψ are updated by

$$\phi^{n+1} = \phi^n - \Delta t (1 + \alpha \Delta t \Delta^2)^{-1} \{ \boldsymbol{v} \cdot \nabla \phi \}^n , \tag{46}$$

$$c^{n+1} = c^n - \Delta t (1 - \alpha \Delta t \Delta)^{-1} \{ \nabla_{\|} \cdot (c \boldsymbol{v}) \}^n , \tag{47}$$

$$\psi^{n+1} = \psi^n - \Delta t (1 + \alpha \Delta t \Delta^2)^{-1} \left\{ v_{\mathrm{bo}} |\nabla \psi| + \frac{\delta \mathcal{H}_{\mathrm{reg}}}{\delta \psi} \right\}^n , \tag{48}$$

where we use periodic boundary conditions set sufficiently far from the interface to guarantee that there are at least 4 grid nodes between the surface and domain boundaries, so that our sixth-order accurate methods for renormalization and extension remain appropriately accurate [15]. The inverse operators are computed using FFT methods.

The algorithm for biphasic vesicle dynamics is then as follows:

1. Initialize the level set functions ϕ, ψ on a three dimensional grid, and then iterate ψ such that contours are geodesics on the surface $\phi = 0$ using the numerical method from [15]. The field c is set to be one everywhere, and D_N and D_n are both set to zero.
2. Repeat the following until either the maximum time or maximum number of iterations is reached:
   i. Calculate the geometry fields using the discretizations from Sec. 4.3.
   ii. Calculate the surface and line force densities $\boldsymbol{f}$ and $\boldsymbol{g}|_{\partial \mathcal{P}}$ without terms from the Lagrange multipliers $\sigma^{\pm}$, P.
   iii. Find the maximum value of $|\boldsymbol{v}|$ near the interface, $v_{\max}$, and use $v_{\max} \Delta t = N_{\mathrm{CFL}} \Delta s$ to determine the time step size Δt. We take the CFL number $N_{\mathrm{CFL}} = 1$ for multiphase vesicle simulations.
   iv. Solve for the Lagrange multipliers $\sigma^{\pm}$, P by specifying $\mathrm{d}V/\mathrm{d}t$, $\mathrm{d}A/\mathrm{d}t$, and $\mathrm{d}A^{-}/\mathrm{d}t$ using Eqs. (8), (9).
   v. Calculate the complete $\boldsymbol{f}$ and $\boldsymbol{g}|_{\partial \mathcal{P}}$. Then find $\boldsymbol{v}$ and v_{bo}.
   vi. Calculate $(\phi^{n+1}, c^{n+1}, \psi^{n+1})$ according to Eqs. (46), (47), (48)
   vii. Reinitialize ϕ if necessary.
   viii. Calculate the maximum of $\left(\Delta s \sqrt{(k_n)^2 + (k_g)^2} \right)$. If this number is larger than 30, stop regularizing ψ using the geodesic algorithm given in [15], and instead set $D_N = 1, D_n = 1$ thereafter and use the regularization Hamiltonian given in Eq. (43). (This specific criterion for the maximum value was found by trial and error with numerical experiments.)

4.3. Discretization of surface geometry in the level set framework

To complete the description of our algorithm, we must define how we compute surface geometric quantities numerically. Given a two dimensional surface $\mathcal{P}$ represented implicitly as the zero level set of $\phi(Z)$, the normal vectors $\boldsymbol{N}$ of the surface are chosen to point into the region where ϕ is positive. The tangential vectors $\boldsymbol{S}_\alpha$ are chosen such that $\boldsymbol{N} \cdot (\boldsymbol{S}_1 \times \boldsymbol{S}_2) > 0$, i.e., $\{\boldsymbol{N}, \boldsymbol{S}_1, \boldsymbol{S}_2\}$ is a right handed coordinate.

We work in Cartesian coordinates and compute first and second derivatives using the standard central difference discretizations on a $3 \times 3 \times 3$ stencil, e.g.

$$\nabla \phi = \frac{(\phi_{i+1,jk} - \phi_{i-1,jk})}{2\Delta x} \hat{\mathbf{x}} + \frac{(\phi_{i,j+1,k} - \phi_{i,j-1,k})}{2\Delta y} \hat{\mathbf{y}} + \frac{(\phi_{ij,k+1} - \phi_{ij,k-1})}{2\Delta z} \hat{\mathbf{z}} \tag{49}$$

$$\nabla^2 \phi = \frac{(\phi_{i+1,jk} - 2\phi_{ijk} + \phi_{i-1,j,k})}{\Delta x^2} + \frac{(\phi_{i,j+1,k} - 2\phi_{ijk} + \phi_{i,j-1,k})}{\Delta y^2} + \frac{(\phi_{ij,k+1} - 2\phi_{ijk} + \phi_{ij,k-1})}{\Delta z^2} . \tag{50}$$

The normal vectors and mean and Gaussian curvatures are then discretized as

$$\boldsymbol{N} = \frac{\nabla\phi}{|\nabla\phi|}\,, \tag{51}$$

$$K_M = -\frac{\nabla^2\phi}{|\nabla\phi|} + \frac{\nabla\phi\cdot\mathbb{H}(\phi)\cdot\nabla\phi}{|\nabla\phi|^3}\,, \tag{52}$$

$$K = \frac{\nabla\phi\cdot\mathbb{K}(\phi)\cdot\nabla\phi}{|\nabla\phi|^4}\,, \tag{53}$$

where the Hessian and curvature matrices are

$$\mathbb{H}(\phi) = \begin{pmatrix} \phi_{xx} & \phi_{xy} & \phi_{xz} \\ \phi_{yx} & \phi_{yy} & \phi_{yz} \\ \phi_{zx} & \phi_{zy} & \phi_{zz} \end{pmatrix}\,, \tag{54}$$

$$\mathbb{K}(\phi) = \begin{pmatrix} \phi_{yy}\phi_{zz}-\phi_{zy}\phi_{yz} & \phi_{zx}\phi_{yz}-\phi_{yx}\phi_{zz} & \phi_{yx}\phi_{zy}-\phi_{zx}\phi_{yy} \\ \phi_{zy}\phi_{xz}-\phi_{xy}\phi_{zz} & \phi_{xx}\phi_{zz}-\phi_{zx}\phi_{xz} & \phi_{zx}\phi_{xy}-\phi_{xx}\phi_{zy} \\ \phi_{xy}\phi_{yz}-\phi_{yy}\phi_{xz} & \phi_{xz}\phi_{yx}-\phi_{xx}\phi_{yz} & \phi_{xx}\phi_{yy}-\phi_{yx}\phi_{xy} \end{pmatrix}\,. \tag{55}$$

The gradient operator $\nabla_\parallel$ on the surface is

$$\nabla_\parallel = \nabla - \boldsymbol{N}(\boldsymbol{N}\cdot\nabla)\,, \tag{56}$$

and, therefore, the surface divergence of a vector field $\boldsymbol{F}$ restricted to the surface is

$$\nabla_\parallel\cdot\boldsymbol{F} = \nabla_i F^i - N_i N^j \nabla_j F^i\,, \tag{57}$$

and the Laplace-Beltrami operator applied to a scalar field F restricted to the surface is

$$\Delta_\parallel F = \nabla_i\nabla^i F - K_M N^i \nabla_i F - N^i N^j \nabla_j \nabla_i F\,. \tag{58}$$

In the level set framework, an integral of a surface field $F(S)$ over the surface can be replaced by an integral over the volume

$$\int_{\mathcal{P}} F(S)\mathrm{d}A = \int_{\Omega} \hat{F}(\boldsymbol{R})\delta(\phi)|\nabla\phi|\mathrm{d}V\,, \tag{59}$$

where $\hat{F}(\boldsymbol{R})$ agrees with $F(S)$ on $\mathcal{P}$ and $\delta(\phi)$ is the Dirac Delta function. The Hausdorff measure (surface area) and Lebesgue measure (volume) of $\mathcal{P}$ is

$$A = |\mathcal{P}(t)| = \int \delta(\phi)|\nabla\phi|\mathrm{d}V\,, \tag{60}$$

$$V = |\Omega(t)| = \int H(-\phi)\mathrm{d}V\,, \tag{61}$$

where $H(-\phi)$ is the Heaviside function. The common practice in the level set method to discretize the Dirac-Delta function and Heaviside function is to smear them out to a bandwidth of $\epsilon = 1.5\Delta x$ around the interface [35]:

$$H(\phi) = \begin{cases} 0 & \phi < -\epsilon \\ \frac{1}{2} + \frac{\phi}{2\epsilon} + \frac{1}{2\pi}\sin\left(\frac{\pi\phi}{\epsilon}\right) & -\epsilon \le \phi \le \epsilon \\ 1 & \epsilon < \phi \end{cases}\,,$$

and

$$\delta(\phi) = \begin{cases} 0 & \phi < -\epsilon \\ \frac{1}{2\epsilon} + \frac{1}{2\epsilon}\cos\left(\frac{\pi\phi}{\epsilon}\right) & -\epsilon \le \phi \le \epsilon \\ 0 & \epsilon < \phi. \end{cases}\,.$$

This discretization, however, can lead to systematic $\mathcal{O}(1)$ errors in trivial numerical experiments, such as computing length of a straight line tilted with respect to the grid axis [46]. Several numerical schemes for approximating $\delta(\phi)$ and $H(\phi)$ have been proposed to address this convergence issue. Engquist proposed using information in the local gradient of the level set function to modify ϵ [47], while Smereka borrowed a technique from Green's function theory to discretize the delta function [48]. In our method, the Dirac Delta function $\delta(\phi)$ and the Heaviside function $H(\phi)$ are discretized by the finite difference method developed by Towers in a series of papers [49,50,41,51]. Following [49], we define $I(\phi) = \int_0^\phi H(\zeta)\mathrm{d}\zeta = \max(\phi, 0)$ on the grid. Then,

$$\nabla I(\phi) = H(\phi)\nabla\phi \,, \tag{62}$$

$$\Delta I(\phi) = \nabla H(\phi)\cdot\nabla\phi + H(\phi)\Delta\phi = \delta(\phi)|\nabla\phi|^2 + H(\phi)\Delta\phi. \tag{63}$$

Solving for $H(\phi)$ and $\delta(\phi)$ from Eq. (62)-(63) gives

$$H(\phi) = \frac{\nabla I\cdot\nabla\phi}{|\nabla\phi|^2} \,, \tag{64}$$

$$\delta(\phi) = \frac{\Delta I(\phi) - H(\phi)\Delta\phi}{|\nabla\phi|^2} = \frac{\Delta I(\phi)}{|\nabla\phi|^2} - \frac{(\nabla I\cdot\nabla\phi)\Delta\phi}{|\nabla\phi|^4}. \tag{65}$$

Mutli-dimensional delta functions [41] can be defined in a similar spirit, using integrals on a codimension $d-m$ manifold Γ represented by the intersection of the zero level sets of m functions $\phi^i, i = 1, 2\cdots m$ in a d-dimensional space parametrized by $Z^i, i = 1, 2\cdots d$

$$\int_\Gamma F(S)\mathrm{d}S = \int_\Omega \hat{F}(Z)\Pi_{i=1}^m \delta(\phi^i(Z))|\wedge_m \nabla\phi^i|\mathrm{d}\Omega \,, \tag{66}$$

where $\mathrm{d}\Omega$ is the invariant volume element in d-dimensional space, S is some parametrization of Γ, $\mathrm{d}S$ is the invariant volume element in Γ, $\hat{F}(Z)$ is defined over Ω, which, when restricted to Γ, agrees with $F(S)$ and $\wedge$ is the wedge product. Consider the case $m = 2, d = 3$, i.e. a curve in space. Let us denote the two level set functions by ϕ and ψ. Then, the Dirac Delta function product $\delta(\phi)\delta(\psi)$ is determined from [41]

$$\nabla H(\phi)\wedge\nabla H(\psi) = \delta(\phi)\delta(\psi)\nabla\phi\wedge\nabla\psi \,,$$

giving

$$\delta(\phi)\delta(\psi) = \frac{(\nabla\phi\wedge\nabla\psi)\cdot(\nabla H(\phi)\wedge\nabla H(\psi))}{|\nabla\phi\wedge\nabla\psi|^2} \,, \tag{67}$$

where $\wedge$ is the vector cross product operator. Convergence of $\delta(\phi)\delta(\psi)$ requires ϕ, ψ to be signed distance functions with their zero level sets orthogonal to each other and their normals parallel to the grid axis [41].

4.4. Discretization of the geometries of lines in the level set framework

Phase boundaries and open edges of membranes can be numerically described as the zero level set of a vector function $(\phi(Z), \psi(Z))$ [52]. Wang implemented this method with a phase field approach in order to simulate multi-component lipid membranes [42]. The Hamiltonian that was used for the phase boundary, however, contained only the zeroth order term from the more general Hamiltonian in Eq. (6), and was therefore unable to describe more realistic effects due to the boundary energy.

To account for the complete force at phase and/or edge boundaries requires an appropriate discretization of the boundary geometry. Following [52], a closed curve Γ embedded in the surface $\mathcal{P} = \{\boldsymbol{R}(Z)|\phi(Z) = 0\}$ is represented by $\Gamma = \{\boldsymbol{R}(Z)|\phi(Z) = 0, \psi(Z) = 0\}$. Then Γ separates $\mathcal{P}$ into two regions corresponding to $\psi > 0$ and $\psi < 0$. We choose the orientation of Γ such that $\psi < 0$ lies to the left, when one moves along the tangential direction $\boldsymbol{t}$ of Γ with their head pointing in the $\boldsymbol{N}$ direction. Furthermore, we choose the direction of the normal $\boldsymbol{n}$ to be pointing into the $\psi > 0$ region. With this convention, $\{\boldsymbol{n}, \boldsymbol{t}, \boldsymbol{N}\}$ forms a right-handed coordinate system. The geometries of Γ can then be expressed in terms of $\phi(Z)$ and $\psi(Z)$, with the unit tangent

$$\boldsymbol{t} = \frac{\nabla\phi\times\nabla\psi}{|\nabla\phi\times\nabla\psi|} \,, \tag{68}$$

and the unit normal

$$\boldsymbol{n} = \boldsymbol{t}\times\boldsymbol{N} \,. \tag{69}$$

The invariant derivatives ∇_s and $\nabla_\perp$ are

$$\nabla_s = t^i\nabla_i \,, \tag{70}$$

$$\nabla_\perp = n^i\nabla_i \,. \tag{71}$$

The geodesic curvature k_g is

$$\begin{aligned} k_g &= \boldsymbol{n}\cdot\nabla_s\boldsymbol{t} = \frac{\boldsymbol{n}}{|\nabla\phi\times\nabla\psi|}\cdot\nabla_s(\nabla\phi\times\nabla\psi) \\ &= \frac{\boldsymbol{n}}{|\nabla\phi\times\nabla\psi|}\cdot(\nabla_s\nabla\phi\times\nabla\psi + \nabla\phi\times\nabla_s\nabla\psi) \,. \end{aligned} \tag{72}$$

where $\nabla_s\nabla\phi$ and $\nabla_s\nabla\psi$ should be calculated as $\nabla_s\nabla\phi = t^j(\nabla_j\nabla^i\phi)\boldsymbol{Z}_i$, $\nabla_s\nabla\psi = t^j(\nabla_j\nabla^i\psi)\boldsymbol{Z}_j$ so that the second derivatives of ϕ, ψ are directly discretized. The normal curvature k_n, geodesic torsion τ_g and $B_\perp$ are given by

$$k_n = -\boldsymbol{t}\cdot\nabla_s\boldsymbol{N} = -t^i t^j \nabla_j N_i \,, \tag{73}$$

$$\tau_g = -\boldsymbol{t}\cdot\nabla_\perp\boldsymbol{N} = -t^i n^j \nabla_j N_i \,, \tag{74}$$

$$B_\perp = -\boldsymbol{n}\cdot\nabla_\perp\boldsymbol{N} = -n^i n^j \nabla_j N_i \,. \tag{75}$$

As can be seen from Eqs. (73)-(75), k_n, τ_g, and $B_\perp$ are components of $\nabla_j N_i$ in the $\{\boldsymbol{t}, \boldsymbol{n}\}$ plane. The tensor $\nabla^j N_i$ can be computed as

$$\nabla^j N_i = \nabla^j\left(\frac{\nabla_i\phi}{|\nabla\phi|}\right) = \frac{1}{|\nabla\phi|^3}(|\nabla\phi|^2\nabla^j\nabla_i\phi - \nabla_i\phi\nabla^k\phi\nabla^j\nabla_k\phi) \,, \tag{76}$$

which can be written in matrix form in Cartesian coordinates as

$$\nabla\otimes\boldsymbol{N} = \frac{\mathbb{H}(\phi)}{|\nabla\phi|} - \frac{1}{|\nabla\phi|^3}\mathbb{H}(\phi)\otimes(\nabla\phi)^\intercal\otimes\nabla\phi \,. \tag{77}$$

From Eq. (66), the integral of a scalar field F over Γ is

$$\int_\Gamma F(s)\mathrm{d}l = \int_\Omega \hat{F}(\boldsymbol{R})\delta(\phi)\delta(\psi)|\nabla\phi\times\nabla\psi|\mathrm{d}V \,, \tag{78}$$

and, in particular, the length of Γ is

$$L(\phi,\psi) = \int_\Omega \delta(\phi)\delta(\psi)|\nabla\phi\times\nabla\psi|\mathrm{d}V \,. \tag{79}$$

5. Results

In this section, we use the algorithm developed in Sec. 4 to explore the dynamics for vesicles under a number of different scenarios. All simulations were carried out on a Navida P100 GPU, and, unless otherwise noted, were performed on a 64^3 Cartesian grid with a time step defined by $N_{CFL} = 0.1$. Standard computation times were ∼10 minutes for single phase vesicle simulations and ∼30 minutes for multi-phase vesicles. We begin by simulating single phase vesicles and explore how changes in the reduced volume, area difference, and spontaneous curvature affect the equilibrium shapes. These simulations are also used to test the convergence of the algorithm. Our results agree well with previous experiments and simulations, while providing a more physical representation of the dynamics and improved convergence. We then explore the dynamics of bi-phasic vesicles and find conditions for which the presence of phase boundaries on a membrane naturally lead to exocytosis/endocytosis of specific phase regions.

5.1. Shape of single phase vesicles

In order to validate the convergence and accuracy of our method, we begin by investigating the shapes and dynamics of single phase vesicles. Here we adopt the area-difference elasticity model [27] for single phase vesicles where the effect of a relative areal stretching of the two monolayers is taken into account. In this model, the Hamiltonian for a closed bilayer vesicle is given by Eq. (7), from which we can compute the elastic bending force,

$$\begin{aligned}\boldsymbol{f} = -\Big\{&\kappa\left(\Delta_\parallel K_M + \frac{1}{2}K_M^3 - 2K_M K + 2CK - \frac{1}{2}C^2 K_M\right)\\ &-\sigma K_M - P - 2\sigma_{\Delta A} hK\Big\}\boldsymbol{N}.\end{aligned} \tag{80}$$

This force is used in Eq. (3) to define the velocity, which is then used to evolve the level set equation using the algorithm described in Sec. 4.1.

We begin by considering the relaxation of axisymmetric ellipsoids with zero spontaneous curvature. For oblate initial conditions, we expect the equilibrium shape to be a discoid, whereas prolate shapes should relax to gourd shapes. The values of the three Lagrange multipliers, P, σ, and $\sigma_{\Delta A}$ are determined by the constraints on the enclosed volume, the surface area, and the area difference between the two bilayer leaflets. Therefore, we set the following conditions at all time steps [28]

$$C = 0 \,, \quad \frac{\mathrm{d}V}{\mathrm{d}t} = \frac{V_p - V(t)}{\Delta t} \,, \quad \frac{\mathrm{d}A}{\mathrm{d}t} = \frac{A_p - A(t)}{\Delta t} \,, \quad \sigma_{\Delta A} = 0 \,, \tag{81}$$

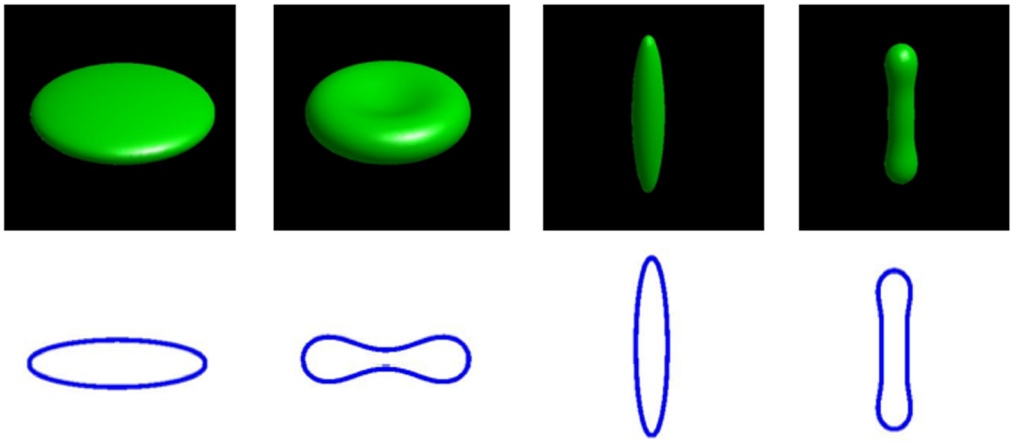

Fig. 3. Relaxation of an oblate ellipsoid (first panel) to a discocyte (second panel) and relaxation of a prolate ellipsoid (third panel) to a gourd (fourth panel). The second row shows a cross-sectional view of the first row. All shapes have reduced volume $v = 0.6$ Simulations shown were performed on a 64^3 grid with $N_{CFL} = 0.1$. The domain was cubic with sides that spanned from -1 to 1, and the initial shape was an ellipsoid with semi-major axis of length 0.7 and semi-minor axis of length 0.181.

Table 1
Final energies, pressures, and surface tensions dependence on grid spacing.

grid sizes	48^3	64^3	80^3	96^3	128^3
total energy	98.008	97.827	98.061	98.150	98.222
pressure, P	−93.41	−101.88	−106.04	−106.07	−106.13
tension, σ	−15.372	−16.246	−16.794	−16.784	−16.763

where $V(t), A(t)$ are the current volume and area of the vesicle, and V_p and A_p are taken to be the initial volume and area of the ellipsoid. The area and volume are computed using Eqs. (60)-(61), with the Heaviside and Dirac delta functions discretized as given in Eqs. (64)-(65). The requirement of Eq. (81) combined with Eqs. (8)-(10) give values of σ, P such that the volume and area of the vesicle remain constant during the simulation. Using a reduced volume $v = 0.6$, we show the initial and equilibriated shapes of an oblate and a prolate ellipsoid (Fig. 3). As expected, the equilibrium shapes are a discocyte and gourd, respectively.

To verify convergence with respect to the spatial discretization, we relaxed an oblate ellipsoid with $v = 0.6$ on grids of size $(48^3, 64^3, 80^3, 96^3, 128^3)$ and computed the bending energy, Lagrange multipliers P and σ, and the relative errors in volume and area as a function of time. We find that the dynamics of each of these quantities are similar on all five grids (Fig. 4). Close inspection of the late-time behavior confirms that the solutions converge as the grid spacing is decreased. The values of the bending energy, P, and σ as a function of grid spacing are given in Table 1. Using the bending energy as a metric, we computed the rate of convergence and found that the error in the energy decreases approximately as the cube of the grid spacing (inset to Fig. 4). The pressure and surface tension show similar behavior (Table 1). We do find that the surface tension Lagrange multiplier σ oscillates for the 96^3 and 128^3 grids (Fig. 4c). We also find that the enclosed volume and surface area are well conserved for all grid sizes, with the best performance on the finest grid (Fig. 4d).

Similarly, we verify convergence in the time discretization by relaxing the $v = 0.6$ oblate ellipsoid on a 98^3 grid using a range of different N_{CFL} values, since our adaptive Δt is computed from $\Delta t = N_{\text{CFL}} \Delta s / v_{\max}$. Here, too, we find that the dynamics for the bending energy and Lagrange multipliers follow similar dynamics regardless of the choice of N_{CFL}, with the smaller time steps leading to smoother behavior (Table 2 and Fig. 5a-c). Using the bending energy as a metric for convergence, we consider the difference between the energy with $N_{CFL} = 0.25$ and $N_{CFL} = 0.1$ and divide this by the difference in energy between the $N_{CFL} = 0.5$ and $N_{CFL} = 0.1$ simulations. This ratio should be equal to

$$\frac{E_{0.25} - E_{0.1}}{E_{0.5} - E_{0.1}} = \frac{2.5^n - 1}{5^n - 1}, \tag{82}$$

where n is the rate of convergence. Using the data in Table 2, we can solve for n, which gives $n \sim 1.5$. Therefore, our algorithm converges at least linearly with the size of the time step, which is what is expected since our formulation computes the velocity of the distance map using the current time step (e.g., see Eq. (41)). We also find that the smaller time steps satisfy the constraint on the enclosed volume and surface area better (Fig. 5d).

In summary, our algorithm, which includes the semi-implicit scheme adopted from [39], maintains convergence when applied to more complicated scenarios, thereby ensuring the accuracy of the shapes obtained in our simulations.

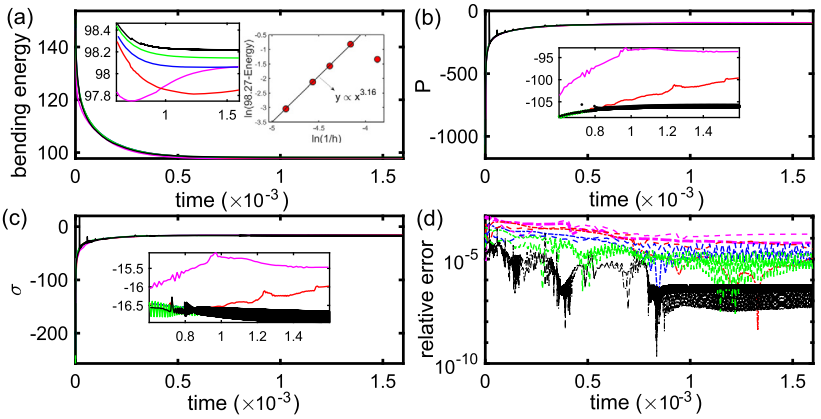

Fig. 4. Spatial convergence for the relaxation of the oblate ellipsoid to a discoid. Bending energy (a) and the Lagrange multipliers for the volume, P (b), and surface area, σ (c), as functions of time for grid sizes 48^3 (magenta), 64^3 (red), 80^3 (blue) 96^3 (green), and 128^3 (black). The insets show an enlarged view of the behavior at later time points, with the second inset in (a) showing the convergence of the energy with grid spacing h, which scales approximately like h^{-3}. (d) The enclosed volume (dashed curves) and surface area (dotted curves) vs time, showing that these quantities are well conserved over the course of the simulations for all grid sizes.

Table 2
Final energies, pressures, and surface tensions dependence on N_{CFL}.

N_{CFL}	0.1	0.25	0.5	1.0
total energy	98.150	98.153	98.160	98.165
pressure, P	−106.07	−106.04	−106.03	−105.98
tension, σ	−16.782	−16.872	−16.955	−16.984

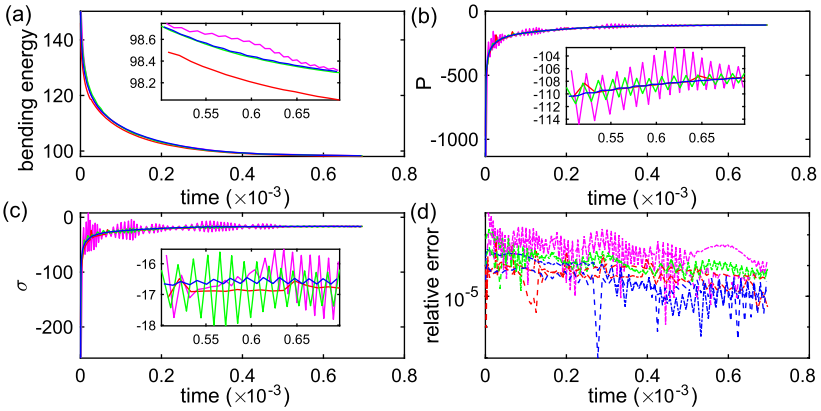

Fig. 5. Temporal convergence for the relaxation of the oblate ellipsoid to a discoid. Bending energy (a) and the Lagrange multipliers for the volume, P (b), and surface area, σ (c), as functions of time for a grid size of 98^3 with N_{CFL} = 1 (magenta), 0.5 (red), 0.25 (green), and 0.1 (blue). The insets show an enlarged view of the behavior at later time points. (d) The enclosed volume (dashed curves) and surface area (dotted dashed curves) vs time, showing that these quantities are well conserved over the course of the simulations for all CFL choices.

5.1.1. Effects of constant spontaneous curvature and osmotic pressure

The dynamics that we have just discussed pertained to vesicles with zero spontaneous curvature. Inclusion of a non-zero spontaneous curvature will have the effect of favoring vesicles with a specific curvature. For example, a large negative spontaneous curvature will try to drive the vesicle to being significantly more curved than the shapes that we found previously. A large spontaneous curvature is then expected to lead to instabilities in shapes that are not sufficiently curved, causing them to form regions of curvature that closer match the preferred curvature. To examine the effect of a large negative spontaneous curvature, we use the same initial conditions as before, with oblate and prolate ellipsoids of reduced volume $v = 0.6$, and set the spontaneous curvature to $C = -30$ (note that in our convention, a unit sphere has $C = -2$). We find that this large spontaneous curvature destabilizes small perturbations in the shape and drives both of these initial conditions to pinch off small vesicles (Fig. 6). In the case of the oblate ellipsoid, standard numerical noise in the simulations is sufficient to initiate the growth of arms off the sides of the ellipsoid (Fig. 6a). At the juncture between the arms and the main body, the membrane then begins to pinch, eventually resulting in the release of a number of smaller vesicles. For the prolate ellipsoid, vesicles instead pinch off at either end, resulting in two small spherical vesicles from the ends, and a

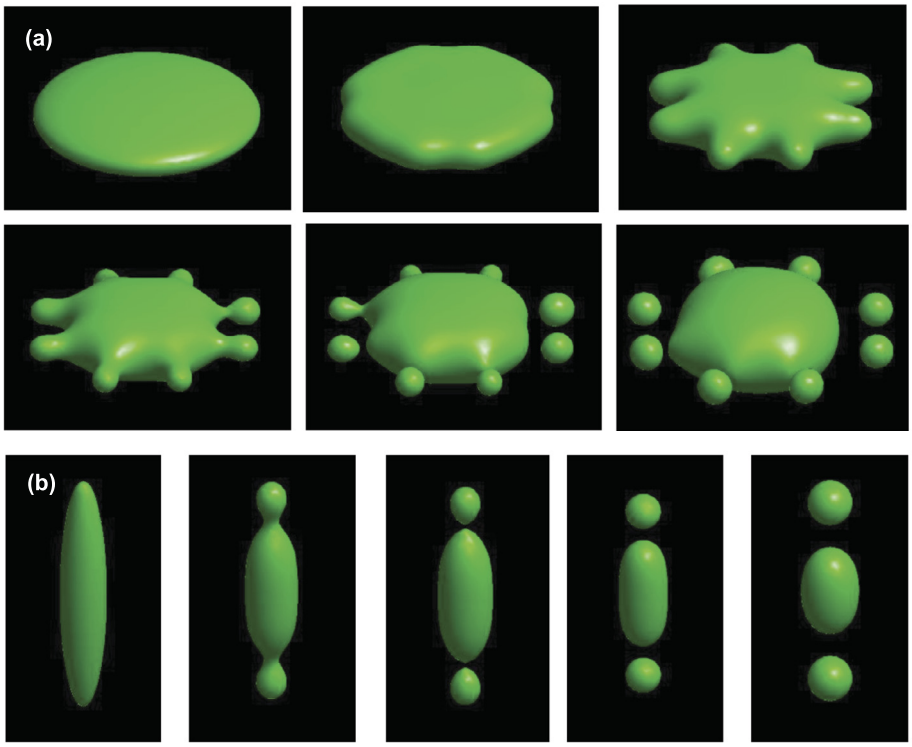

Fig. 6. Shape evolution of an oblate (a) and prolate (b) ellipsoid with $v = 0.6$ and spontaneous curvature $C = -30$. (a) The oblate ellipsoid transforms into a starfish-type shape, and then the arms pinch off into small spherical vesicles. (b) For the prolate ellipsoid, each end vesiculates into a small sphere, leaving a larger ellipsoidal vesicle in the center. Simulations shown were performed on a 64^3 grid with $N_{CFL} = 0.1$.

larger central vesicle in the middle (Fig. 6b). These simulations also demonstrate that curvature-driven topological changes can be handled seamlessly using our implementation of the level set method, even in three dimensional space.

While there are many cases where vesicles have a fixed enclosed volume, it is also possible to experimentally alter the volume of a vesicle by adjusting the external osmotic conditions (i.e., the osmotic pressure) [53]. We explore the effects of a nonzero spontaneous curvature and a constant osmotic pressure by setting $P = P_0 = \text{constant}$ and $\sigma_{\Delta A} = \sigma_{\Delta A_0} = \text{constant}$. Note that a constant $\sigma_{\Delta A} = \sigma_{\Delta A_0}$ is equivalent to a constant spontaneous curvature $C = -\sigma_{\Delta A_0} h/\kappa$, with a shifted surface tension $\sigma \to \sigma + \frac{\kappa}{2} C^2$. Therefore, the spontaneous curvature and the Lagrange multiplier for the leaflet area difference are not independent parameters, and the effects of a constant spontaneous curvature can be simulated either by specifying the value of C or the value of $\sigma_{\Delta A}$. In other words, both C and $\sigma_{\Delta A}$ can be interpreted as *generalized forces* with the area difference between the bilayer as *generalized displacements*.

We can then explore how varying the osmotic conditions affects the shape of a vesicle with constant spontaneous curvature by fixing the osmotic pressure P and the Lagrange multiplier for the area difference $\sigma_{\Delta A}$. Specifically, we use the following conditions in our single-phase vesicle algorithm:

$$C = 0\,, \quad P = P_0\,, \quad \frac{\mathrm{d}A}{\mathrm{d}t} = \frac{A_p - A(t)}{\Delta t}\,, \quad \sigma_{\Delta A} = \sigma_{\Delta A_0}\,, \tag{83}$$

where A_p is set to be the initial area and $A(t)$ is the current area. Requiring Eq. (83) to be satisfied, while imposing Eqs. (8)-(10) leads to a value for σ that conserves the surface area.

The effects of these two parameters can lead to a vast range of different types of shapes. For example, if we start with an initial condition of a prolate ellipsoid with reduced volume $v = 0.5$ and set $P = -2000$ and $\sigma_{\Delta A_0} = 0$, the large negative pressure causes the vesicle to reduce its volume. It does this by stretching out into a longer rod-shaped vesicle with hemispherical end caps, as shown in Fig. 7a. If we instead start with an oblate ellipsoid with $v = 0.4$ and set $P_0 = -1000$ and $\sigma_{\Delta A_0} = 13$, deflation of the vesicle by the negative pressure causes the vesicle to flatten into more of a disk shape, while the spontaneous curvature induced by $\sigma_{\Delta A_0}$ tries to round up the vesicle at the edges. The shape eventually pinches in the center and undergoes a topological change to a toroidal shape (Fig. 7b). An interesting example of how a modest change in parameters leads to a qualitatively different shape is seen when we start with an oblate ellipsoid with $v = 0.75$ under a smaller pressure $P_0 = -200$ (Fig. 7c). If we set ($\sigma_{\Delta A_0} = 12$ the ellipsoid transitions into a 3-armed starfish shape (Fig. 7c (top panel)), while setting $\sigma_{\Delta A_0} = 20$ favors larger curvatures and therefore leads to a 4-armed starfish shape (Fig. 7c (bottom panel)).

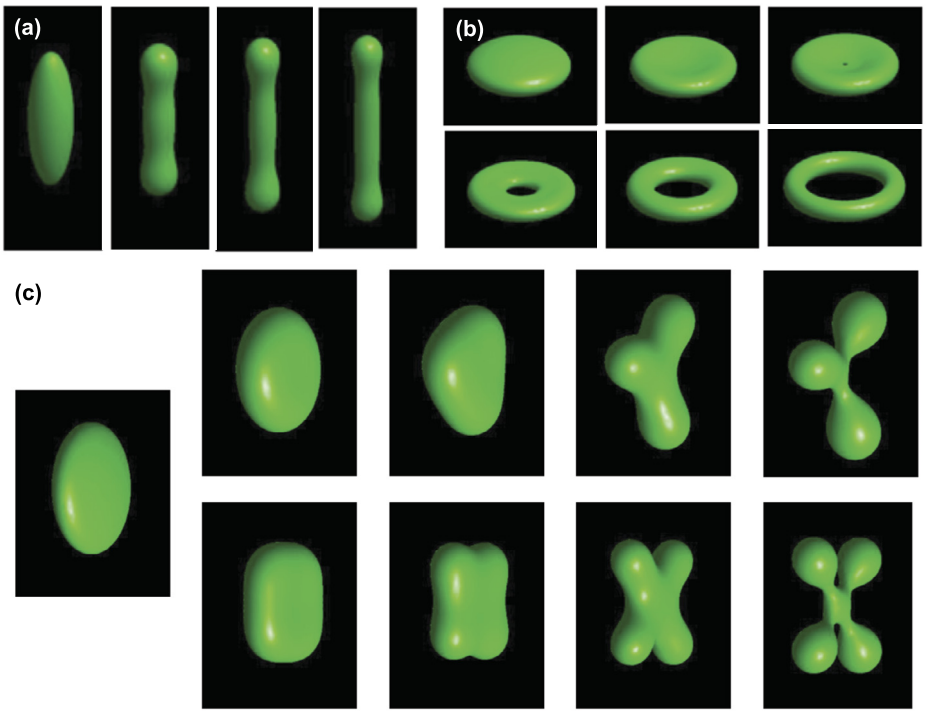

Fig. 7. Relaxation of a few representative shapes under the conditions of constant osmotic pressure and non-zero spontaneous curvature. (a) A prolate ellipsoid with $v = 0.5$, $P_0 = -2000$, and $\sigma_{\Delta A_0} = 0$ relaxes to a rod shape with hemispherical end caps. (b) An oblate ellipsoid with $v = 0.4$, $P_0 = -1000$, and $\sigma_{\Delta A_0} = 13$, undergoes a topological transition and relaxes to a toroidal shape, while (c) an oblate ellipsoid with $v = 0.75$, $P_0 = -200$, and $\sigma_{\Delta A_0} = 12$ (top) or $\sigma_{\Delta A_0} = 20$, becomes either a 3-armed (top) or 4-armed (bottom) starfish shape. Simulations were performed on a 64^3 grid with $N_{CFL} = 0.1$.

5.1.2. Relaxation under constrained reduced area difference

Varying the values of P_0 and $\sigma_{\Delta A_0}$ in the previous section, we obtained shapes of different reduced volumes and reduced area differences. We can also constrain the reduced area difference using the Lagrange multiplier method by setting

$$C = 0, \frac{\mathrm{d}V}{\mathrm{d}t} = \frac{V_p - V(t)}{\Delta t}, \frac{\mathrm{d}A}{\mathrm{d}t} = \frac{A_p - A(t)}{\Delta t}, \frac{\mathrm{d}(\Delta a)}{\mathrm{d}t} = \eta_\varepsilon\left(\frac{\Delta a_p - \Delta a(t)}{\Delta t}\right),$$

where Δa_p is the prescribed reduced area difference, Δa is the current reduced area difference, and $\eta_\varepsilon(\xi) = \begin{cases} \xi & \mathrm{abs}(\xi) \leqslant \varepsilon \\ \mathrm{sign}(\xi)\cdot\varepsilon & \mathrm{abs}(\xi) > \varepsilon \end{cases}$, where ε is a small positive constant limiting the time rate of change of the reduced area difference. The physical difference between this methodology and the one used in the previous section is that here the volume, area, and area difference are constrained to be approximately constant throughout the simulation, whereas in the former method the volume and area difference can vary while the osmotic pressure and area difference Lagrange multipliers are held constant. Therefore, these represent two different dynamical conditions that can lead to different equilibrium states.

In order to determine some of the shapes that are possible from these constraints, we first consider an initial condition of an oblate spheroid with $v = 0.6$ and $\Delta a = 1.05$ and relax it with $\Delta a_p = \Delta a =$ constant. As shown in Fig. 8a, this initial condition causes the ellipsoid to deform into a triangular disk with rounded edges. The dynamics are somewhat interesting, as the vesicle initially takes on a shape with four sides, before transitioning into the triangular shape. If we instead start with a prolate ellipsoid with $v = 0.9$, $\Delta a = 1.05$, and $\Delta a_p = 1.10$, then the vesicle loses symmetry along the long axis and deforms into a pear (Fig. 8b). Starting with a oblate ellipsoid with $v = 0.55$, $\Delta a = 1.06$, and $\Delta a_p = 1.22$, the vesicle begins forming the precursors to eight arms, but eventually goes to a squarish-shaped disk with one side having an invaginated region (Fig. 8c). This shape is sometimes called a two-armed starfish shape. If we instead consider a prolate ellipsoid with $v = 0.55$ and set $\Delta a = 1.47$ and $\Delta a_p = 1.60$, the ellipsoid evolves into a necklace shape (Fig. 8d). An interesting transformation occurs if we start with the triangular disk-shape that resulted in Fig. 8a. Changing the parameters such that $v = 0.8$, $\Delta a = 1.04$, and $\Delta a_p = 0.9$, the final shape is a stomatocyte with an inward invagination at the center of one of the wide sides (Fig. 8e).

5.1.3. Summary of single phase vesicles

Here we have shown that our algorithm provides an accurate and convergent scheme for handling the relaxation dynamics of single phase vesicles. Our results for the shapes that are obtained for specific reduced volume, surface area, and area differences are consistent with experimental results [54] and some previous numerical simulations [55]. For example,

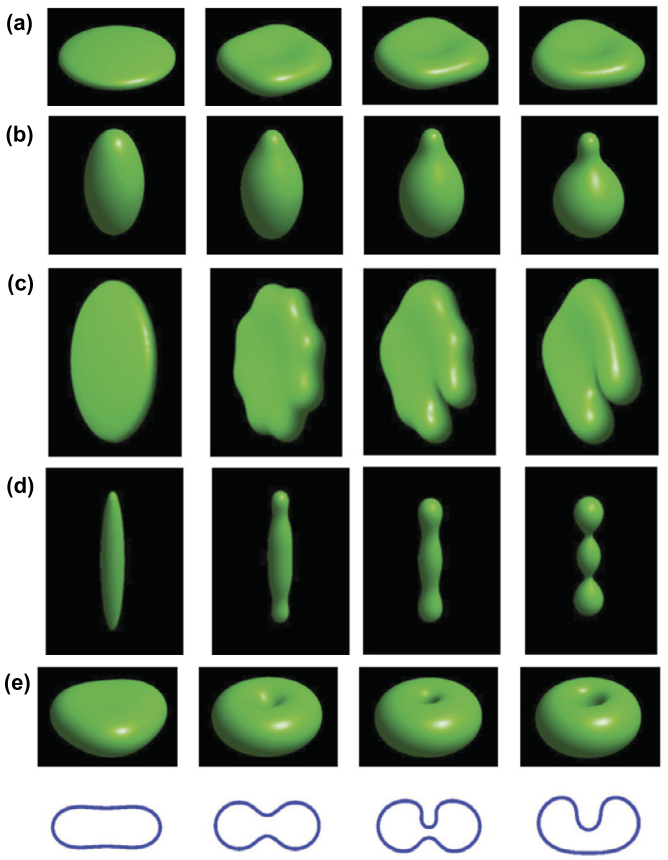

Fig. 8. Dynamics under the action of the area difference constraint. (a) An initially oblate ellipsoid with $v = 0.6$ and $\Delta a = \Delta a_p = 1.05$ relaxes to a rounded-edged, triangular disk. (b) Relaxation of an initially prolate ellipsoid with $v = 0.9$, $\Delta a = 1.05$, and $\Delta a_p = 1.10$ to a pear shape. (c) A two-armed starfish shape arises from an initially oblate ellipsoid with $v = 0.55$, $\Delta a = 1.06$, and $\Delta a_p = 1.22$. (d) An initially prolate ellipsoid with $v = 0.55$, $\Delta a = 1.47$, and $\Delta a_p = 1.60$ transforms into a necklace shape. (e) A stomatocyte is obtained from the relaxation of a triangular disk subject to $v = 0.8$, $\Delta a = 1.04$, and $\Delta a_p = 0.9$. Simulations were performed on a 64^3 grid with $N_{CFL} = 0.1$.

these previous works have determined the phase diagram for the dependence of vesicle shape on v and Δa [54,55], which our results agree well with. In addition, some of the shapes that we have determined, such as the four-armed starfish (Fig. 7c) have been observed in experiments [53], but are not included in the experimental or numerical phase diagrams. It is also important to note that the aforementioned numerical simulations use the Surface Evolver package to find the minimum energy configurations, which uses a general gradient descent approach, which does not necessarily model the physical dynamics of the system and cannot be used to study vesicles that are out of equilibrium. Our algorithm shows how asymmetrical shapes, such as starfishes, triangular elliptocytes, pears, stomatocytes, etc. arise naturally from initially symmetrical shapes through the action of a resistive force theory.

5.2. Shape of multi-component vesicles

We now turn to the case of heterogeneous vesicles that contain regions with distinct phases separated by sharp boundaries. Experimentally, lipid domains can be produced from mixtures of high melting temperature (saturated) lipids, low melting temperature (unsaturated) lipids, and cholesterol [6]. Because of its hydrophobic steroid ring structure, cholesterol does not fit in either the solid-ordered phase of the saturated lipids (due to its peculiar size and shape) or the Ld (lipid-disordered) phase of the unsaturated lipids (due to its hydrophobicity). As such, a third lipid phase arises in the presence of cholesterol, which maintains fluidity and allows rapid diffusion in the plane of the membrane, while also featuring conformational order in the lipid chains that increases rigidity and stability of the membrane [56]. This third phase is the *Lo (lipid-ordered) phase* [56]. Lipid-ordered domains have many similarities with lipid-rafts found in vivo [3], which are important in many membrane functions.

Theoretical and numerical studies of multi-domain vesicles began as early as the 1990s. Jülicher and Lipowky seem to be the first to propose a Hamiltonian for multidomain vesicles which takes into account the effects of different Gaussian bending moduli within the different phase domains [57]. Taniguchi performed numerical studies of phase separation dynamics and shape deformation of two component vesicles [58]. Jülicher and Lipowky's theory was then confirmed by Baumgart's

experiments [25]. Recently, phase field methods were adapted to perform the numerical simulation of multicomponent vesicles [42,59,60]. Our level set approach is the first three dimensional simulation of multicomponent vesicles that takes into account the differences in Gaussian bending moduli and can easily add in forces from the more general line Hamiltonian (Eq. (6)). In our simulation, vesicle shape evolves according to mechanical forces that arise directly from the variation of the Hamiltonian (3.3), while the driving forces calculated in the phase-field model are not derived explicitly from the variation of the Hamiltonian, but rather are only thermodynamically consistent [42,59].

5.2.1. Hamiltonian of an incompressible biphasic vesicle

Consider a vesicle with patches of Ld and Lo phases that are denoted by $\mathcal{P}^-$ and $\mathcal{P}^+$, respectively. These regions are defined by two distance maps ψ and ϕ as described in Sec. 4.2 and given by

$$\begin{aligned}\mathcal{P}^- &= \{\boldsymbol{R}(Z)|\phi(Z)=0,\psi(Z)<0\}\,,\\ \mathcal{P}^+ &= \{\boldsymbol{R}(Z)|\phi(Z)=0,\psi(Z)>0\}\,.\end{aligned} \tag{84}$$

Thus $\boldsymbol{n}$ points into $\mathcal{P}^+$ from $\mathcal{P}^-$. The Hamiltonian for a biphasic vesicle can be written as

$$\begin{aligned}\mathcal{H}_{\rm bi} = &\int_{\mathcal{P}^-} \mathrm{d}A\left[\frac{\kappa^{\rm Ld}}{2}(K_M - C^{\rm Ld})^2 + \kappa_G^{\rm Ld}K\right] + \sigma^-\left(\int_{\mathcal{P}^-}\mathrm{d}A - A^-\right)\\ &+\int_{\mathcal{P}^+} \mathrm{d}A\left[\frac{\kappa^{\rm Lo}}{2}(K_M - C^{\rm Lo})^2 + \kappa_G^{\rm Ld}K\right] + \sigma^+\left(\int_{\mathcal{P}^+}\mathrm{d}A - A^+\right)\\ &-P\left(\int\frac{\boldsymbol{R}\cdot\boldsymbol{N}}{3}\mathrm{d}A - V_p\right) + \int\mathrm{d}A\frac{\mu}{2}\left[(1-c)^2 + \left(1-\frac{1}{c}\right)^2\right]\\ &+\oint_{\partial\mathcal{P}^-}\mathrm{d}l(\kappa_l + \kappa_g k_g + \kappa_\tau\tau_g + \kappa_n k_n)\,,\end{aligned} \tag{85}$$

where $\kappa^{\rm Ld(Lo)}$ and $\kappa_G^{\rm Ld(Lo)}$ are the mean curvature and Gaussian curvature bending moduli for the Ld (Lo) phase, $C^{\rm Ld(Lo)}$ is the spontaneous curvature for the Ld (Lo) phase, $\sigma^{-(+)}$ is the Lagrange multiplier that enforces conservation of the area $A^{-(+)}$ of the Ld (Lo) phase, P constrains the volume of the vesicle, and $\kappa_{l,g,\tau,n}$ can be interpreted as line tension constants associated with curve length, geodesic curvature, geodesic torsion and normal curvature. As mentioned previously, the c field in Eq. (85) enforces local incompressibility of the membrane.

It is important to note that the addition of the field c introduces new terms into the calculation of the variation of the Hamiltonian. Under a variation $\boldsymbol{R}\to\boldsymbol{R}+\delta\boldsymbol{R}$, the lipid density field $c\to c+\delta c$ and an infinitesimal area $\mathrm{d}A\to\mathrm{d}A+\delta(\mathrm{d}A)$. In a given patch of membrane, the total number of lipids does not change under the variation. Therefore,

$$\delta c = -c\frac{\delta(\mathrm{d}A)}{\mathrm{d}A} = -(\nabla_\alpha W^\alpha - W K_M)c\,, \tag{86}$$

where we have ignored the second order term $\delta c\delta(\mathrm{d}A)$. If we then consider a Hamiltonian that is only a function of the field c, $f(c)$, such as in Eq. (45), we find that this function produces an effective surface tension

$$\sigma_c = f(c) - c\frac{\partial f}{\partial c}\,. \tag{87}$$

The biphasic vesicle Hamiltonian, Eq. (85), then leads to a surface bending force $\boldsymbol{f}_{\rm su}$ and line forces $\boldsymbol{g}_{\rm bo}$ located at the phase boundary

$$\begin{aligned}\boldsymbol{f}_{\rm su} = &-\kappa\left(\Delta_\parallel K_M + \frac{1}{2}K_M^3 - 2K_M K + 2CK - \frac{1}{2}C^2K_M\right)\boldsymbol{N}\\ &+\nabla_\parallel\sigma_c - [(\sigma+\sigma_c)K_M + P]\,\boldsymbol{N}\,,\end{aligned} \tag{88}$$

$$\begin{aligned}\boldsymbol{g}_{\rm bo} = &(\kappa^{\rm Ld}-\kappa^{\rm Lo})\nabla_\perp K_M\boldsymbol{N} - \left[\frac{\kappa^{\rm Ld}}{2}(K_M - C^{\rm Ld})^2 - \frac{\kappa^{\rm Lo}}{2}(K_M - C^{\rm Lo})^2\right]\boldsymbol{n}\\ &-\left\{\left(\frac{\kappa_G^{\rm Ld}-\kappa_G^{\rm Lo}}{2} + \kappa_g\right)(K\boldsymbol{n} + \nabla_s\tau_g\boldsymbol{N}) + (\sigma^- - \sigma^+)\boldsymbol{n}\right\} + \kappa_l(k_g\boldsymbol{n} + k_n\boldsymbol{N})\\ &+\kappa_\tau[(\nabla_s k_g - k_n\tau_g)\boldsymbol{N} - (\nabla_s k_n + k_g B_\perp)]\boldsymbol{n} + k_n[(\nabla_s\tau_g + k_g B_\perp)\boldsymbol{n} + \tau_g^2\boldsymbol{n}]\,,\end{aligned} \tag{89}$$

Table 3
Final energies from simulation on different grids.

grid sizes	48^3	64^3	80^3
total energy	122.138	123.786	124.095
line energy	86.282	88.190	88.021
bending energy for Ld phase	14.637	14.366	14.508
bending energy for Lo phase	21.219	21.230	21.566

where

$$\kappa \equiv \kappa^{\mathrm{Lo}} H(\psi) + \kappa^{\mathrm{Ld}}(1 - H(\psi)) ,$$
$$C \equiv C^{\mathrm{Lo}} H(\psi) + C^{\mathrm{Ld}}(1 - H(\psi)) ,$$
$$\sigma \equiv \sigma^{+} H(\psi) + \sigma^{-}(1 - H(\psi)) ,$$

with $H(\psi)$ the Heaviside function of ψ. Note that the presence of κ_g is equivalent to a difference in Gaussian bending moduli across the phase boundary, κ_G^{Ld} and κ_G^{Lo}, which is a natural result of the Gauss-Bonnet theorem.

The normal speed v_{N} of the surface is determined from the balance of the bending force and the viscous force in the $\boldsymbol{N}$ direction,

$$(\boldsymbol{f}_{\mathrm{su}} + \delta(\psi)|\nabla\psi|\boldsymbol{g}_{\mathrm{bo}}) \cdot \boldsymbol{N} = \zeta_{\mathrm{bi}} v_{\mathrm{N}} , \tag{90}$$

where the coefficient $\delta(\psi)|\nabla\psi|$ localizes the line force to the surface. We also take the viscosity coefficient ζ_{bi} to be one for simplicity. The normal speed v_{bo} of the phase boundary is determined from the balance of forces in the $\boldsymbol{n}$ direction,

$$\boldsymbol{g}_{\mathrm{bo}} \cdot \boldsymbol{n} = \xi_{\mathrm{bi}}(v_{\mathrm{bo}} - v_{\mathrm{sn}}) , \tag{91}$$

where the viscosity coefficient ξ_{bi} is set to be one, and v_{sn} is the $\boldsymbol{n}$ component of the surface velocity, which is determined from

$$\boldsymbol{f}_{\mathrm{su}} \cdot \boldsymbol{n} = \zeta_{\mathrm{bi}} v_{\mathrm{sn}} . \tag{92}$$

The velocities that are derived from these forces are then implemented into our multiphase algorithm described in Sec. 4.2, which allows us to track the dynamics of these vesicles by simulating the motion of the fields ϕ, ψ, and c. It is worth pointing out that we do not include $\boldsymbol{g}_{\mathrm{bo}}$ directly in the velocity of the c field; however, we do assume that $\boldsymbol{g}_{\mathrm{bo}}$ induces a tension jump of $(\sigma^- - \sigma^+)$ between the Ld and Lo phases. This jump in tension leads to changes in c via compression or stretching of the vesicle (see Eq. (86)), and those effects are included in the dependence of $\boldsymbol{f}_{\mathrm{su}}$ on $\sigma^{\pm}$. In a more realistic hydrodynamical model, the line force density $\boldsymbol{g}_{\mathrm{bo}}$ will give rise to a locally varying tension field with jumps at the phase boundaries instead of two constant tensions $\sigma^{\pm}$ with different phases. This makes it difficult for us to conserve the area of small domains when we consider the presence of multiple phase regions. Still, many interesting simulations can be carried out within this very simple framework, and more physically consistent models can be explored in the future.

5.2.2. Deformation of a two domain biphasic vesicle

We begin our analysis of multiphase vesicles by considering a vesicle with a single phase boundary between an Ld and an Lo phase. We start with the simplest assumption that the phase boundary has an associated line tension κ_l, which we set to be 30, and that the only other non-zero material parameters are $\kappa^{\mathrm{Ld}} = \kappa^{\mathrm{Lo}} = 1$. The vesicle is initialized to be a sphere with the Ld phase (colored in red in Fig. 9) covering 20% of the area. We set the reduced volume to be 0.90, and the Lagrange multipliers are determined using

$$\frac{\mathrm{d}V}{\mathrm{d}t} = \eta_\varepsilon \left(\frac{V_p - V(t)}{\Delta t} \right) , \quad \frac{\mathrm{d}A}{\mathrm{d}t} = \frac{A_p - A(t)}{\Delta t} , \quad \frac{\mathrm{d}A^-}{\mathrm{d}t} = \frac{A_p^- - A^-(t)}{\Delta t} ,$$

at each time step, where $V(t)$, $A(t)$, and $A^-(t)$ are the current volume, current total area, and current area of the Ld phase. The prescribed volume is $V_p = 0.9V(0)$ and $A_p = A(0)$, $A^-(t) = A^-(0)$, and ε is a small number limiting the time rate of change of the volume. We are thus conserving total area and the area of each of the phases in our simulation, while allowing the volume to decrease until the prescribed volume is reached. As can be seen from Fig. 9, the Ld phase bulges out due to the line tension, introducing a kink at the phase boundary. This simple example verifies that our algorithm is able to simulate the deformations of a membrane under the actions of a locally applied line tension, while tracking the boundary between the two phases as it is driven by the forces in the system. The resulting shape is also in qualitative agreement with the shapes that are observed experimentally in biphasic vesicles [61]. By starting with different phase distributions and changing simulation parameters, we are able to explore effects that arise from various physical origins.

To validate the convergence of our simulations as the grid spacing is refined, we ran simulations using the same parameters as in the preceding simulation with grids of size 48^3, 64^3, and 80^3. We computed the final shape and energy for each

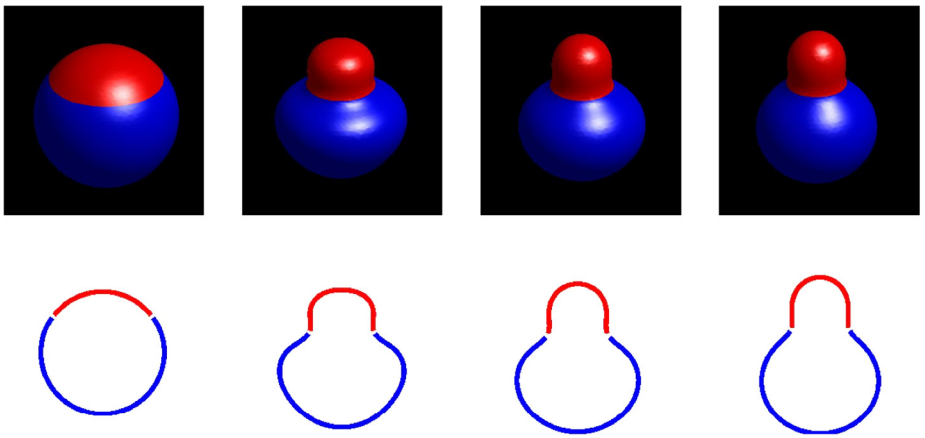

Fig. 9. Deformation of a two domain biphasic vesicle driven by a line tension. The red and blue regions denote the Ld and Lo domains, respectively. An initially spherical vesicle that has a patch of Ld that occupies 20% of the membrane area, produces a bulged Ld region due to contraction at the phase boundary driven by the line tension, which is set to $\kappa_l = 30$. Simulations were performed on a 64^3 grid with $N_{CFL} = 0.1$ and $\kappa^{\mathrm{Lo}} = \kappa^{\mathrm{Ld}} = 1$. All other material parameters in the Hamiltonian were zero.

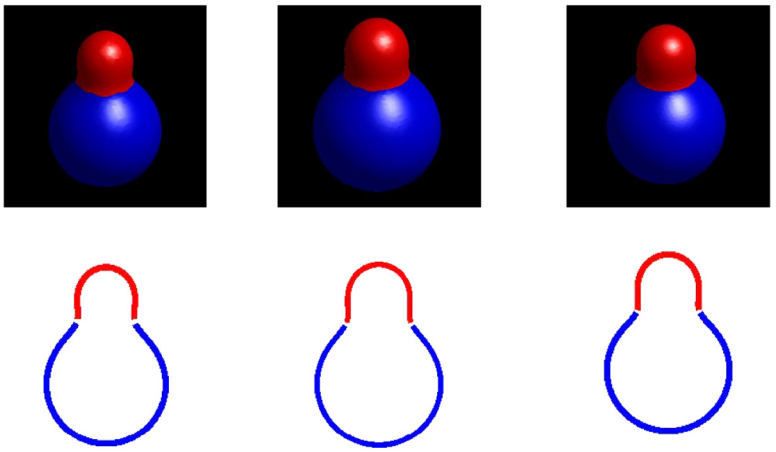

Fig. 10. Final shapes for a biphasic vesicle of reduced volume $v = 0.9$ with a single Ld phase region that occupies 20% of the surface area. The material parameters are the same as in Fig. 9. Top panels show the 3D view and the bottom panels show a cross sectional view of the vesicle at the same numerical time for grids of size 48^3 (left), 64^3 (middle), and 80^3 (right).

case. For each of these grids, the final shapes at a simulation time of 0.021 are nearly indistinguishable (Fig. 10). The energy provides a more quantitative comparison. As shown in Table 3, the final total energy, line energy, and bending energies for the Ld and Lo phases are also in good agreement, highlighting that even the 48^3 grid is sufficient to resolve the dynamics of these vesicles.

5.2.3. Pinching of biphasic bidomain vesicles

In this section, we explore conditions under which a two domain biphasic vesicle will pinch. In particular, we examine which of the following physical quantities are most crucial for driving the vesiculation of a biphasic vesicle: a prescribed reduced volume, a constant spontaneous curvature, or the line tension at the phase boundary constant κ_l.

For a biphasic vesicle with two domains where the fraction of the surface area for the Ld phase is r, it is straightforward to show that the maximum reduced volume $v_{\max}(r)$ for which the vesicle will pinch into two parts is $(1-r)^{3/2} + r^{3/2}$, which gives, $v_{\max}\left(\frac{1}{2}\right) = \frac{2}{\sqrt{2}}$ when $r = 0.5$. Thus, if the prescribed final reduced volume is larger than $\frac{2}{\sqrt{2}}$, the vesicle will not pinch for any value of the line tension. This result is illustrated in Fig. 11, where we show the **final** shape of vesicles with different prescribed reduced volume v_p and line tension κ_l. The only nonzero material parameters are $\kappa^{\mathrm{Ld}} = \kappa^{\mathrm{Lo}} = 1$ and κ_l. We consider two scenarios. First, $v_p = 0.8 > \frac{2}{\sqrt{2}}$ (Fig. 11 (top panel)), where changing the line tension from a value of 5 to a value of 30, results in a decrease in the radius at the juncture between the two phases, but never results in separation of the vesicle into two parts. However, if we instead consider a reduced volume of $v_p = 0.7$ and change the line tension from 4 to 10, we find a substantially smaller neck region for values of $\kappa_l = 4$ or 5 than was seen in the previous case for any value of the line tension (Fig. 11 (bottom panel)). Furthermore, when $\kappa_l = 10$, the vesicle splits into two vesicles

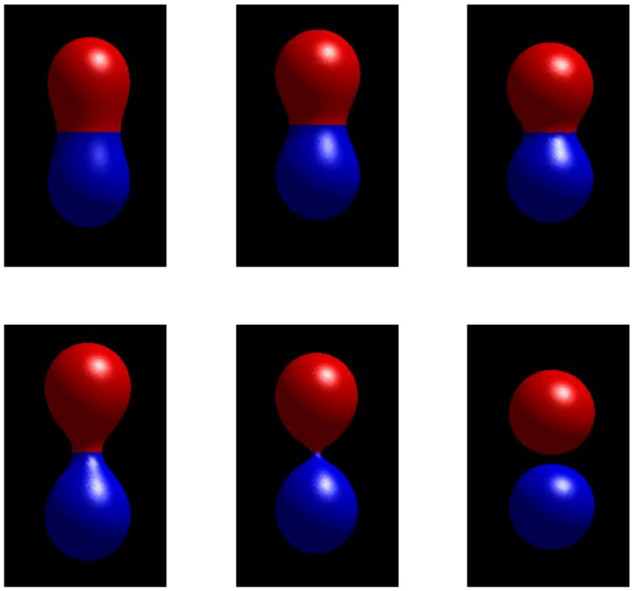

Fig. 11. Equilibrium shapes for biphasic vesicles with a prescribed reduced volume v_p and line tension κ_l. The top row shows the equilibrium shapes when $v_p = 0.8$ for $\kappa_l = 5$ (left), 10 (middle), and 30 (right). The line tension is never able to break the vesicle into two parts for this case. Conversely, when $v_p = 0.7$ (bottom row), values of $\kappa_l = 4$ (left) or 5 (middle) cause a much larger deformation at the phase boundary than was seen when $v_p = 0.8$, and when $\kappa_l = 10$ (right), the equilibrium shape is one where each phase has broken into its own vesicle. Simulations used a 64^3 grid with $\kappa^{\mathrm{Lo}} = \kappa^{\mathrm{Ld}} = 1$ and $N_{CFL} = 0.1$.

at the phase boundary. Even though Fig. 11 shows **final** shapes of vesicles with different v_p and κ_l, we may also regard the progression from left to right in this figure as representing the **dynamical** shape transformations with increasing line tension.

Next we study the effects of a constant spontaneous curvature C on the two-domain biphasic vesicle. In order to test how changing the spontaneous curvature affects the shape, we start by equilibriating the shape of the biphasic vesicle with $v_p = 0.7$, $\kappa_l = 4$ or 5, and the spontaneous curvatures set to zero, $C^{\mathrm{Ld}} = C^{\mathrm{Lo}} = 0$. We then begin simulations from these initial shapes but with a non-zero value of the spontaneous curvatures, $C^{\mathrm{Ld}} = C^{\mathrm{Lo}} = -5$ or -10. These simulations mimic the dynamics where curvature-inducing proteins rapidly bind to the membrane, changing the effective spontaneous curvature. As is shown in Fig. 12 (top row), when we start with the previous scenario where $v_p = 0.7$ and $\kappa_l = 5$, which produced a dumbell shaped vesicle with a fairly small neck region, a spontaneous curvature of -5 causes the neck to pinch and the two different phase regions into separate in individual vesicles. Decreasing the line tension to $\kappa_l = 4$, however, prevents the vesicles from fully separating (Fig. 12 (middle row)). Increasing the induced spontaneous curvatures to -10 causes the neck region to pinch off (Fig. 12 (bottom row)). Thus adding curvature inducing proteins may have a destabilizing effect that allows narrow neck regions to fully scission.

The above numerical experiments show that the reduced volume v_p, fraction of the area covered by each phase r (e.g., the membrane area occupied by lipid rafts), the line tension κ_l, and the spontaneous curvature C all play meaningful roles in the pinching of biphasic vesicles. A complete exploration of the effects from all of the parameters in Eqs. (5), (6) warrants examination but is beyond the scope of the current paper.

5.2.4. Pinching of multidomain biphasic vesicles

In our simulations of bidomain vesicles, we found that it was not necessary to impose the incompressibility condition described in Sec. 4.2 as long as the area fraction for each phase was constrained using the Lagrange multiplier approach. For multidomain vesicles, however, incompressibility becomes necessary if we want to prevent nonphysical changes of domain sizes. For example, we first consider a spherical vesicle at time zero that has twelve circular Ld regions with a smaller bending modulus than the Lo region. The material parameters we use are $\kappa^{\mathrm{Ld}} = 1, \kappa^{\mathrm{Lo}} = 10, \kappa_l = 20$ (Fig. 13a (top left panel)). At the beginning of the simulation, we set the volume constraint to be $V_p = 0.9V(0)$ and simulate the dynamics without enforcing the local inextensibility condition (i.e., setting $\mu = 0$). For this case, the vesicle starts shrinking, allowing the line tension to pinch the Ld domains into small bulges on the surface. However, as the simulations progress, four of the Ld regions begin to grow in area, at the expense of the other eight domains (Fig. 13a). By the end of the simulation, the vesicle is a flattened disk with four Ld regions that form evenly-spaced, hemispherical protrusions on the sides. Previous authors have seen similar effects, but attributed the behavior to Oswald ripening [42]. Our results suggest that this is more of an artifact coming from not properly imposing the local inextensibility condition. Indeed, if we instead do the exact same simulation but with $\mu = 1000$, then we find that the vesicle undergoes the same initial shrinking that leads to the echinocytic shape with twelve Ld regions. However, this shape persists as the final equilibrium shape of the vesicle

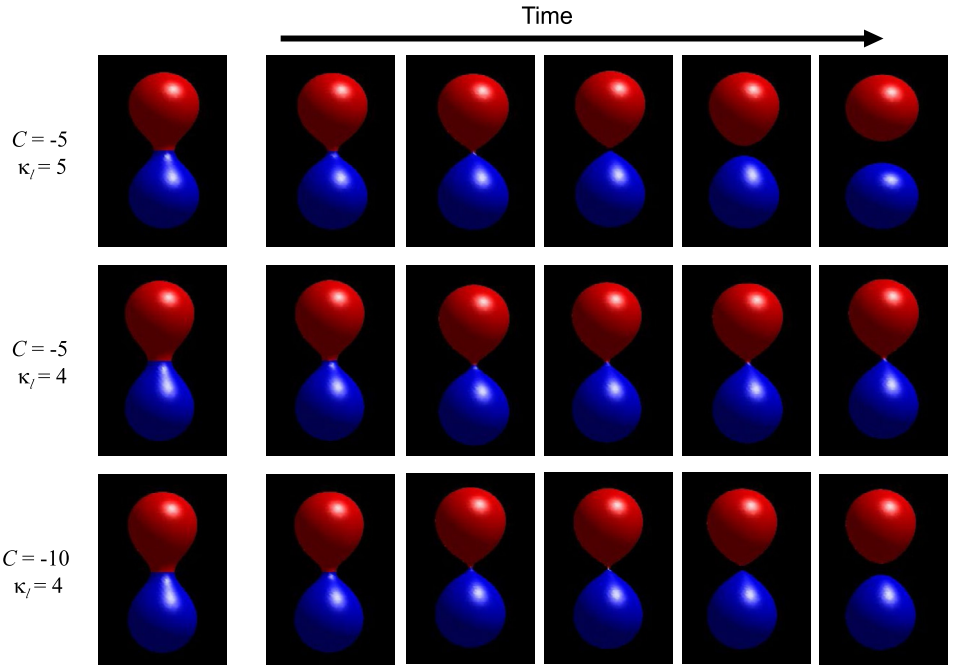

Fig. 12. Temporal evolution of biphasic vesicles with nonzero spontaneous curvature and $v_p = 0.7$ and $r = 0.5$. The left column shows the initial shapes, which were generated by simulating a biphasic, bidomain vesicle with $v_p = 0.7$, $C^{\mathrm{Ld}} = C^{\mathrm{Lo}} = 0$ and $\kappa_l = 4$ or 5 (as noted) up to the point where the vesicle's volume reached the prescribed value. Then, at time zero, the spontaneous curvature was set to $C^{\mathrm{Ld}} = C^{\mathrm{Lo}} = -5$ or -10, leading to the time evolution shown here. Simulations were performed on a 64^3 grid with $\kappa^{\mathrm{Lo}} = \kappa^{\mathrm{Ld}} = 1$ and $N_{CFL} = 0.1$.

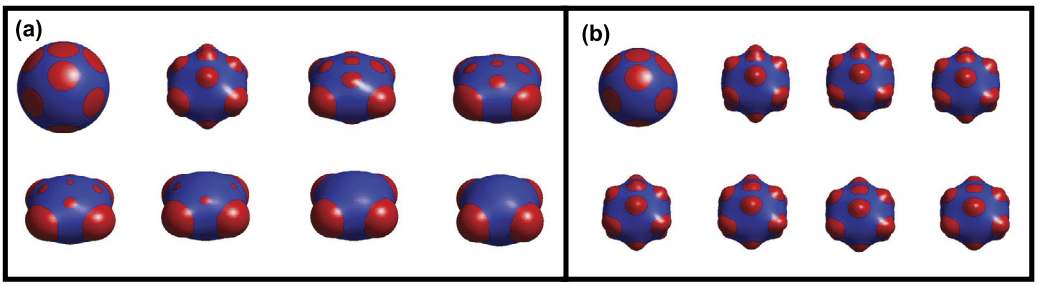

Fig. 13. The dynamics of multidomain, biphasic vesicles and the importance of local incompressibility. An initially spherical vesicle with a continuous Lo phase (blue) and 12 Ld patches (red) is subject to an osmotic change that reduces the reduced volume from one to $v = 0.9$. (a) When the local incompressibility condition is not imposed ($\mu = 0$), eight of the Ld domains shrink at the expense of the other four. (b) Conversely, imposing the incompressibility condition by setting $\mu = 1000$, we find that the twelve domains remain stable. The resulting shape is a roughly spherical vesicle with hemispherical bumps at each Ld domain. The material parameters for both simulations are $\kappa^{\mathrm{Ld}} = 1, \kappa^{\mathrm{Lo}} = 10, \kappa_l = 20$. Grid size = 64^3 and $N_{CFL} = 0.1$.

((Fig. 13b). It is important to note that domain shrinking and coarsening is not completely eliminated in Fig. 13b, but is greatly reduced. A better way to impose the incompressibility would be to solve for a local tension that enforces that the surface divergence of the velocity field is zero. This is currently under investigation.

The dynamics of multi-domain vesicles is of course dependent on the material properties of the membrane. If we consider the same initial condition as in the last two simulations, but with the bending moduli of the two domains flipped so that the Ld regions are stiffer than the Lo domains, $\kappa^{\mathrm{Ld}} = 10$, $\kappa^{\mathrm{Lo}} = 1$, $\kappa_l = 20$, and $\mu = 1000$, while also imposing a larger osmotic change with $V_p = 0.8V(0)$, we find two interesting differences from the previous simulation. First, because the Ld regions are stiffer and the spontaneous is zero, there is a tendency for the Ld regions to flatten out (Fig. 14), as opposed to the bulging that was observed before (Fig. 13b). Second, because we are driving the membrane to a smaller volume, the Ld regions get closer together and can merge, which occurs when a narrow neck forms between two of the Ld regions. The line tension then acts to pull these regions together into a more circular domain, similar to the merging of oil droplets in water. The fusion of domains along with the large bending moduli of the Ld phase drives the vesicle shape to be more and more planar. In the second half of the simulation, some nonphysical shrinking of the domains on the sides is observed, even though we are using the same incompressibility constraint as was used before ($\mu = 1000$).

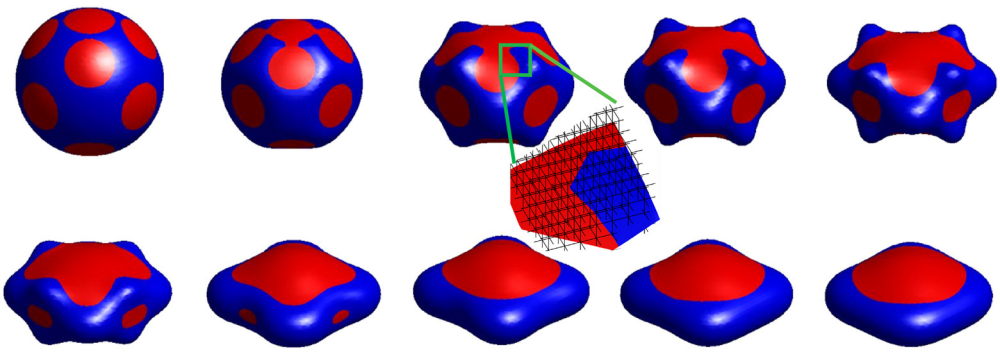

Fig. 14. Phase domain fusion driven by osmotic pressure. An initially spherical vesicle with a continuous Lo phase (blue) with a small bending modulus $\kappa^{\text{Lo}} = 1$ and 12 stiffer Ld patches (red) with $\kappa^{\text{Ld}} = 10$ is subject to an osmotic change that reduces the reduced volume from one to $v = 0.8$. The line tension between the phases is $\kappa_l = 20$. As the vesicle shrinks, the Ld phase domains get closer together and eventually fuse. Some artificial domain shrinking is observed during the simulation. The third panel includes a zoomed in region showing how the phase boundaries are resolved on the grid (shown in black). Other parameters are the same as in Fig. 13.

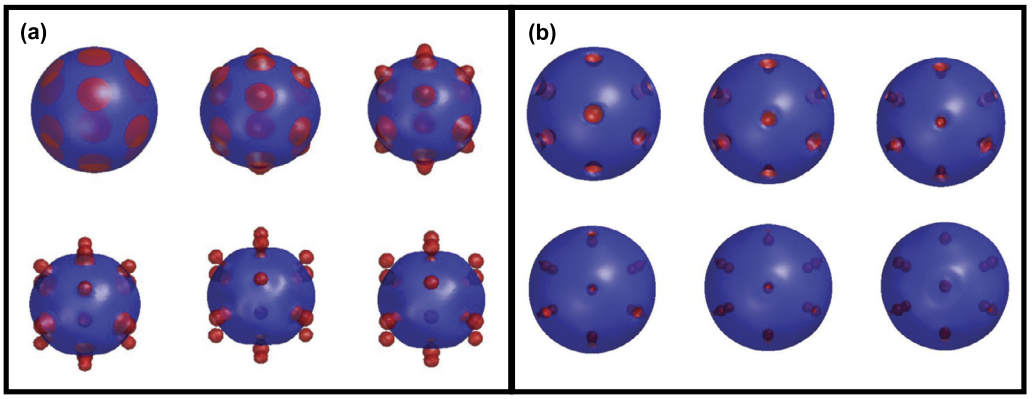

Fig. 15. Exocytosis or endocytosis of phase domains of a biphasic vesicle driven by osmotic pressure. We simulate an initially spherical biphasic vesicle that is driven to shrink by either decreasing the reduced volume to $v = 0.8$ (a), which causes external budding of the vesicles, or by imposing a large negative pressure $P = -600$ (b), which produces internally budded vesicles. The color scheme is the same as in Fig. 14, and the material parameters are $\kappa^{\text{Ld}} = \kappa^{\text{Lo}} = 1$, $\kappa_l = 100$, and $\mu = 1000$. Simulations were performed on a 64^3 grid with $N_{CFL} = 0.1$.

Our final numerical examples are inspired by experiments from [53], where phase separated vesicles were subjected to a change in external osmotic pressure. These experiments observed budding of vesicles from the phase separated regions. Depending on the experimental conditions, it was possible to induce external budding of the vesicles out into the fluid (similar to the beginning stages of exocytosis) or internal budding into the lumen of the vesicle (mimicking endocytosis). We use simulations similar to those previously described to explore this process with our algorithm. Specifically, we set $V_p = 0.8V(0)$, $\kappa^{\text{Ld}} = \kappa^{\text{Lo}} = 1$, $\kappa_l = 100$, and $\mu = 1000$. Under these conditions, we find external budding of the vesicles (Fig. 15a), which is qualitatively similar to the partial pinching of vesicles in Fig. 2a of [53]. In order to maintain stability in these simulations, we used the maximum line curvature of the phase boundary to detect imminent pinching of domains, by calculating $\max\sqrt{((k_n)^2 + (k_g)^2}$ near the phase boundary. When this number is larger than $30/\Delta x$, where Δx is the grid spacing, we stop using the geodesic algorithm from [15] to normalize ψ, and instead set $D_N = 1$, $D_n = 1$ thereafter, and use the method described in Sec. 4.2. As mentioned previously, using this secondary method for normalizing ψ provides more stability in cases where there are large line curvatures at the interfaces between phases.

In experiments, internal budding of the vesicles was induced by subjecting the vesicles to a large osmotic pressure prior to phase separation [53]. To model this, we set the pressure $P = -600$, instead of using the Lagrange multiplier method to enforce a specific reduced volume. We also let the phase separated domains invaginate inward at the start of the simulation. Under these conditions, the vesicle shrinks and the Ld phase regions bud further into the internal lumen of the vesicle (Fig. 15), similar to the experimental observation depicted in Fig. 2b of [53].

5.2.5. Summary of multiphase vesicles

By adjusting the values of different parameters and starting with different initial conditions, we are able to explore the effects of the line tension constant κ_l, bending moduli, prescribed reduced volume, spontaneous curvature, and osmotic pressure on the dynamics of multiphase vesicles. Our simulations not only show that our algorithm can handle these

nontrivial problems in phase separated vesicles, but we also find good agreement between our simulations and experiments. As mentioned, the shape we find for two domain vesicles (e.g., Fig. 11) match well the pear-like shapes that are observed experimentally [61]. Furthermore, we are able to simulate conditions that represent experimental conditions that lead to external or internal vesiculation and get qualitatively similar results to the observations (Fig. 15, [53]). Because we have derived a general description of the forces that can account for a broad spectrum of physical effects (such as differences in Gaussian bending moduli κ_g between the phases, or other line tension parameters, e.g., κ_τ, κ_n), our algorithm opens the door to exploring a range of novel physical conditions involved in multiphase vesicle dynamics. A thorough analysis of the complete line energy (Eq. (6)) is beyond the scope of the current paper and will be presented elsewhere. Still, our numerical scheme integrates different physical forces more naturally than that of [42], allows more parameters to be explored, and seamlessly captures topological changes in the vesicle shape.

6. Conclusions

The dynamics of membranes and vesicles is exceedingly important in cell biology and other areas, such as drug delivery [1,62]. However, the forces that result from even simple, homogeneous energy functionals, such as the Helfrich Hamiltonian [21] are nonlinear and include fourth order spatial derivatives, making numerical simulation of the physics computationally challenging both in regards to stability as well as convergence. In biological applications, the bilayer membrane is often heterogeneous, including phase separated regions such as lipid rafts [2], further complicating accurate modeling of these systems.

Here we have sought to address these challenges from two different avenues. First, from the theoretical side, a heterogeneous membrane consisting of multiple lipid species and transmembrane proteins is expected to be described by an energy functional that is more complex than the Helfrich energy, likely including spatial variation of material parameters and a more complicated dependence on geometric properties of the membrane shape. In addition, phase separation in the membrane will produce boundaries with additional energetic contributions along them. Since the Hamiltonian should only depend on geometric invariants of the membrane shape, the types of allowable terms in the Hamiltonian are limited. Building off the work of [30,31], we are then able to compute all possible forces that can arise from an arbitrary membrane energy functional. Therefore, our theoretical results provide a general description of the forces that could arise in a very broad range of membrane dynamic problems.

Second, we have constructed an algorithm that can stably and accurately solve for the dynamics that arise from generalized membrane forces. This algorithm is based in the level set method, allowing it to handle topological changes in a straightforward manner while also providing a convenient method for describing phase boundaries on the membrane surface as the intersection of two level set functions. In order to create a convergent scheme for handling the high order derivatives that arise in membrane bending forces, we implement our recent sixth-order accurate method for reinitializing the distance map and extending fields away from the zero contour. The semi-implicit method for evolving the level set equation developed by Smereka [39] provides stability to our routine.

We then applied this algorithm to a number of representative cases involving single- and multi-phase vesicles. We showed that the algorithm is convergent and that it is able to reproduce the phase diagram for the shapes of single phase vesicles as a function of the reduced volume and area difference. Then, we examined the case of multiphase vesicles under a number of different scenarios. These simulations produced shapes similar to what have been seen in a number of experiments, and also showed that our algorithm can simulate experimental conditions that lead to the budding of vesicles, both internally and externally.

The general Hamiltonian that we use in this paper includes a wealth of material parameters. The simulations that we carried out here merely scratch the surface of the possible cases that can and should be explored. Our algorithm provides a means to begin to further address the full phase space possible for vesicle dynamics and to explore many other biological and technological applications thereof.

CRediT authorship contribution statement

Tiankui Zhang: Conceptualization, Formal analysis, Investigation, Methodology, Software, Validation, Visualization, Writing – original draft, Writing – review & editing. **Charles W. Wolgemuth:** Conceptualization, Formal analysis, Investigation, Methodology, Supervision, Validation, Visualization, Writing – original draft, Writing – review & editing.

Declaration of competing interest

The authors declare that they have no known competing financial interests or personal relationships that could have appeared to influence the work reported in this paper.

Acknowledgements

This research was partially supported by NIH grant R01 GM114675.

Appendix A. Variations of the metrics and the curvature tensor

The variation of the metrics are found using Eq. (21):

$$\delta S_{\alpha\beta} = \nabla_\alpha W_\beta + \nabla_\beta W_\alpha - 2W B_{\alpha\beta} \,, \tag{A.1}$$

$$\delta S^{\alpha\beta} = -(\nabla^\alpha W^\beta + \nabla^\beta W^\alpha - 2W B^{\alpha\beta}) \,, \tag{A.2}$$

$$\delta S = 2S(\nabla_\alpha W^\alpha - W K_M) \,. \tag{A.3}$$

Likewise, the variation of the curvature tensor is

$$\begin{aligned}\delta B_{\alpha\beta} &= -\delta(\boldsymbol{S}_\beta \cdot \nabla_\alpha \boldsymbol{N}) \,, \\ &= -\delta \boldsymbol{S}_\beta \cdot \nabla_\alpha \boldsymbol{N} - \boldsymbol{S}_\beta \cdot \nabla_\alpha \delta \boldsymbol{N} \,, \\ &= B_\alpha^\gamma \nabla_\beta W_\gamma + B_{\alpha\nu} \nabla_\beta W^\nu + B_{\beta\nu} \nabla_\alpha W^\nu \\ &\quad - B_{\beta\gamma} B_\alpha^\gamma W + \nabla_\alpha \nabla_\beta W \,.\end{aligned} \tag{A.4}$$

The variations of the metrics for a curve embedded in the membrane are

$$\delta U_{\Phi\Psi} = 2\varepsilon_\Phi \varepsilon_\Psi \boldsymbol{t} \cdot \nabla_s \boldsymbol{W} = 2U_{\Phi\Psi} \boldsymbol{t} \cdot \nabla_s \boldsymbol{W} \,, \tag{A.5}$$

$$\delta U = e^\Phi e^\Psi \delta U_{\Phi\Psi} = 2U \boldsymbol{t} \cdot \nabla_s \boldsymbol{W} \,, \tag{A.6}$$

$$\delta \varepsilon^\Phi = -\varepsilon^\Phi \boldsymbol{t} \cdot \nabla_s \boldsymbol{W} \,, \tag{A.7}$$

$$\delta \varepsilon_\Phi = \varepsilon_\Phi \boldsymbol{t} \cdot \nabla_s W \,. \tag{A.8}$$

Appendix B. Example cases of the forces that arise from variations in the generalized Hamiltonian

In this appendix, we compute a number of representative examples for forces that arise from the generalized Hamiltonian given by Eqs. (5)–(6).

B.1. Variations of terms involving area integrals in $\mathcal{H}$

Example 1 *(Variation of the surface area).* The surface area of patch $\mathcal{P}$ is $A = \int_\mathcal{P} \mathrm{d}A$, and the functional derivative is

$$-\frac{\delta A}{\delta \boldsymbol{R}} = \int_\mathcal{P} (K_M \boldsymbol{N}) \mathrm{d}A + \int_{\partial\mathcal{P}} (-\boldsymbol{n}) \mathrm{d}A \,. \tag{B.1}$$

Therefore, an energy of the form $\int_\mathcal{P} \gamma \mathrm{d}A$, where γ is a constant, leads to the following forces per area and length,

$$\begin{aligned}\boldsymbol{f} &= \gamma K_M \boldsymbol{N} \,, \\ \boldsymbol{g}|_{\partial\mathcal{P}} &= -\gamma \boldsymbol{n} \,.\end{aligned} \tag{B.2}$$

The force per area $\boldsymbol{f}$ can be interpreted as a surface tension.

Example 2 *(Variation of the enclosed volume).* The enclosed volume V of a closed surface $\mathcal{P}$ is $V = \frac{1}{3} \oiint_\mathcal{P} \boldsymbol{R} \cdot \boldsymbol{N} \mathrm{d}A$ and

$$-\frac{\delta V}{\delta \boldsymbol{R}} = \oiint_\mathcal{P} (-\boldsymbol{N}) \mathrm{d}A \,.$$

Forces due to turgor pressure or constraints on the enclosed volume are therefore directed in the normal direction $\boldsymbol{N}$.

Example 3 *(Variations of an energy depending on powers of the mean curvature).* To compute the forces from an energy that depends on the nth power of the mean curvature, we consider variations of an energy of the form $\int_\mathcal{P} \frac{\kappa(S)}{n} (K_M)^n \mathrm{d}A$, where n is a positive integer and $\kappa(S)$ is a locally varying bending modulus for the mean curvature. The resulting forces per area and length are

$$\begin{aligned}\boldsymbol{f} &= \boldsymbol{N} \left[\kappa \left(2K_M^{n-1} K - \frac{n-1}{n} K_M^{n+1} \right) - \Delta_\parallel (\kappa K_M^{n-1}) \right] + \frac{K_M^n}{n} \nabla_\parallel \kappa \,, \\ \boldsymbol{g}|_{\partial\mathcal{P}} &= \boldsymbol{N} \nabla_\perp (\kappa K_M^{n-1}) - \left(\frac{\kappa}{n} K_M^n \right) \boldsymbol{n} \,,\end{aligned} \tag{B.3}$$

where we assumed $\delta\kappa = 0$ when computing the variation. When $n = 2$, Eqs. (B.3) reduce to that for the Helfrich Hamiltonian.

Example 4 *(Variation of the Gaussian curvature energy).* For energies that depend on powers of the Gaussian curvature, we compute variations of an energy functional $\int_{\mathcal{P}} \frac{\kappa(S)}{n} K^n \mathrm{d}A$, where n is a positive integer and $\kappa(S)$ is the locally varying bending modulus for the Gaussian curvature. Then

$$\begin{aligned}
\boldsymbol{f} &= \boldsymbol{N}\left[B^{\alpha\beta}\nabla_\alpha\nabla_\beta(\kappa K^{n-1}) - \frac{n-1}{n}\kappa K^n K_M - K_M\Delta_\parallel(\kappa K^{n-1})\right] + \frac{K^n}{n}\nabla_\parallel\kappa \\
\boldsymbol{g}|_{\partial\mathcal{P}} &= \boldsymbol{N}[k_n\nabla_\perp(\kappa K^{n-1}) - \nabla_s(\kappa K^{n-1}\tau_g) - \tau_g\nabla_s(\kappa K^{n-1})] - \left(\kappa\frac{K^n}{n}\right)\boldsymbol{n}\,,
\end{aligned} \tag{B.4}$$

where we have again assumed that $\delta\kappa = 0$. Note that if $n = 1$ and $\kappa = 1$, the variation in the energy simplifies to

$$-\frac{\delta\int_{\mathcal{P}} K\mathrm{d}A}{\delta\boldsymbol{R}} = \oint_{\partial\mathcal{P}}\{-\nabla_s\tau_g\boldsymbol{N} - K\boldsymbol{n}\}\mathrm{d}l\,, \tag{B.5}$$

where the surface integral term disappears as a result of the Gauss-Bonnet theorem, which is why the Gaussian bending energy is often ignored. However, for vesicles with varying Gaussian bending moduli, which can be a result of phase separation and coexistence or varying lipid and protein species, the elastic forces from the Gaussian curvature energy are generally non-zero.

Example 5 *(Variation of $K_M^n K^m$).* Another possibility is that the energy depends on some combination of powers of the mean and Gaussian curvatures, in which case we need to compute the variation of $\int_{\mathcal{P}} \frac{\kappa(S)}{nm} K_M^n K^m \mathrm{d}A$, where n and m are positive integers. Because we can write the variation as

$$\begin{aligned}
\delta\int_{\mathcal{P}}\frac{\kappa}{nm}K_M^n K^m\mathrm{d}A = &\int_{\mathcal{P}}\frac{\kappa K^m}{m}\delta\left(\frac{K_M^n}{n}\mathrm{d}A\right) + \int_{\mathcal{P}}\frac{\kappa K_M^n}{n}\delta\left(\frac{K^m}{m}\mathrm{d}A\right) \\
&- \int_{\mathcal{P}}\frac{\kappa}{nm}K_M^n K^m\delta(\mathrm{d}A)\,,
\end{aligned} \tag{B.6}$$

the forces that arise from an energy such as this are a combination of the results from Eq. (B.3) with $\kappa \to \frac{\kappa K^m}{m}$, Eq. (B.4) with $\kappa \to \frac{\kappa K_M^m}{m}$, and Eq. (28) with $f \to \frac{\kappa}{nm}K_M^n K^m$.

Example 6 *(Variation of $\nabla_\alpha K_M \nabla^\alpha K_M$).* For energies that depend on the gradient of the mean curvature, we compute the variation of $\int_{\mathcal{P}} \frac{\kappa(S)}{2}\nabla_\alpha K_M\nabla^\alpha K_M \mathrm{d}A$. The resulting forces per area and length are

$$\begin{aligned}
\boldsymbol{f} &= \boldsymbol{N}\left[-(K_M^2 - 2K)\nabla^\alpha(\kappa\nabla_\alpha K_M) - \Delta_\parallel\nabla^\alpha(\kappa\nabla_\alpha K_M) + \frac{\kappa}{2}K_M\nabla_\alpha K_M\nabla^\alpha K_M\right] \\
&\quad + \nabla_\parallel\left(\frac{\kappa}{2}\nabla_\alpha K_M\nabla^\alpha K_M\right) \\
\boldsymbol{g}|_{\partial\mathcal{P}} &= \boldsymbol{N}\left[-\kappa(K_M^2 - 2K)\nabla_\perp K_M - \nabla_s^2(\kappa\nabla_\perp K_M) + \nabla_\perp\nabla^\alpha(\kappa\nabla_\alpha K_M)\right] \\
&\quad - \nabla_\perp K_M\nabla_\parallel K_M - \frac{\kappa\boldsymbol{n}}{2}\nabla_\alpha K_M\nabla^\alpha K_M\,.
\end{aligned} \tag{B.7}$$

B.2. Variation of terms involving line integrals in $\mathcal{H}$

Example 7 *(Variation of curve length).* The length of the boundary curve $\partial\mathcal{P}$ is $l = \oint_{\partial\mathcal{P}}\mathrm{d}l$. Then setting $f = 1$ in Eq. (38) gives

$$-\frac{\delta l}{\delta\boldsymbol{R}} = \oint_{\partial\mathcal{P}}(\nabla_s\boldsymbol{t})\mathrm{d}l = \oint_{\partial\mathcal{P}}(k_g\boldsymbol{n} + k_n\boldsymbol{N})\mathrm{d}l\,. \tag{B.8}$$

From Eq. (B.8), the line energy σl will give rise to line tension $\sigma(k_g\boldsymbol{n} + k_n\boldsymbol{N})$ along the boundary curve.

Example 8 *(Variation of the geodesic curvature energy).* Consider the line integral of the function $f = \frac{\kappa}{n}k_g^n$, where n is a positive integer and $\kappa(U)$ can vary along the curve. The resulting force per length along the curve is

$$\boldsymbol{g}|_{\partial\mathcal{P}} = -\nabla_s^2(\kappa k_g^{n-1}\boldsymbol{n}) - \nabla_s\left(\frac{2n-1}{n}\kappa k_g^n \boldsymbol{t}\right) - \kappa k_g^{n-1} k_n n^\alpha \boldsymbol{S}^\beta B_{\alpha\beta}\,. \tag{B.9}$$

For the case where $n=\kappa=1$, the variation $-\frac{\delta\oint k_g \mathrm{d}l}{\delta \boldsymbol{R}} = \oint_{\partial\mathcal{P}} \mathrm{d}l\{-\nabla_s^2\boldsymbol{n} - \nabla_s(\kappa_g\boldsymbol{t}) + k_n n^\alpha \boldsymbol{S}^\beta B_{\alpha\beta}\}$ simplifies to

$$-\frac{\delta\oint k_g \mathrm{d}l}{\delta \boldsymbol{R}} = \oint_{\partial\mathcal{P}} \{-\nabla_s\tau_g \boldsymbol{N} - K\boldsymbol{n}\}\mathrm{d}l\,. \tag{B.10}$$

As expected from the Gauss-Bonnet theorem $\int_{\mathcal{P}} K\mathrm{d}A - \oint_{\partial\mathcal{P}} k_g \mathrm{d}l = 2\pi\chi(\mathcal{P})$, where $\chi(\mathcal{P})$ is the Euler characteristic of $\mathcal{P}$, the right hand sides of Eq. (B.5) and Eq. (B.10) are the same. Eq. (B.10) also agrees with the result from Capovilla [32] and Tu [33].

Example 9 *(Variation of the normal curvature energy).* For a line energy $\oint_{\partial\mathcal{P}} \frac{\kappa}{n}(k_n)^n \mathrm{d}l$, where n is a positive integer and $\kappa(U)$ can vary along the curve, the resulting force per length is

$$\boldsymbol{g}|_{\partial\mathcal{P}} = \kappa k_n^{n-1} k_g B_{\alpha\beta}\boldsymbol{S}^\beta n^\alpha - \nabla_s^2(\kappa k_n^{n-1}\boldsymbol{N}) - \nabla_s\left(\frac{2n-1}{n}\kappa k_n^n \boldsymbol{t}\right)\,. \tag{B.11}$$

For the case $n=\kappa=1$, the variation $-\frac{\delta\oint_{\partial\mathcal{P}}\kappa_n \mathrm{d}l}{\delta\boldsymbol{R}} = \oint_{\partial\mathcal{P}}\{k_g B_{\alpha\beta} n^\alpha \boldsymbol{S}^\beta - \nabla_s^2\boldsymbol{N} + \nabla_s(k_n\boldsymbol{t})\}\mathrm{d}l$ simplifies to give

$$\boldsymbol{g}|_{\partial\mathcal{P}} = -(k_g B_\perp + \nabla_s\tau_g)\boldsymbol{n} - \tau_g^2\boldsymbol{N}\,. \tag{B.12}$$

Example 10 *(Variation of the geodesic torsion energy).* For an energy that is a line integral of a power function of the geodesic torsion, $f = \frac{\kappa}{n}(\tau_g)^n$, where n is a positive integer and $\kappa(U)$ can vary along the curve, then resulting force per length is

$$\begin{aligned}\boldsymbol{g}|_{\partial\mathcal{P}} = &-\nabla_s\left[\kappa\tau_g^{n-1}\left(k_n\boldsymbol{n} + \frac{n-1}{n}\tau_g\boldsymbol{t}\right)\right] + B_{\alpha\beta}\boldsymbol{S}^\beta\nabla_s(\kappa\tau_g^{n-1}n_\alpha)\\ &-\boldsymbol{N}\nabla_s[t_\alpha\nabla_s(\kappa\tau_g^{n-1}n_\alpha)]\,.\end{aligned} \tag{B.13}$$

When $n=\kappa=1$, the variation reduces to $-\frac{\delta\oint_{\partial\mathcal{P}}\frac{\kappa}{n}\tau_g^n \mathrm{d}l}{\delta\boldsymbol{R}} = \oint_{\partial\mathcal{P}}\{-\nabla_s(k_n\boldsymbol{n}) + B_{\alpha\beta}\boldsymbol{S}^\beta\nabla_s n_\alpha - \nabla_s(t_\alpha\nabla_s(n_\alpha))\boldsymbol{N}\}\mathrm{d}l$, giving

$$\boldsymbol{g}|_{\partial\mathcal{P}} = -(\nabla_s k_n + k_g\tau_g)\boldsymbol{n} + (\nabla_s k_g - k_n\tau_g)\boldsymbol{N}\,. \tag{B.14}$$

Example 11 *(Variation of $B_\perp$).* Finally, for a line integrand $f = B_\perp$, the force per length is

$$\boldsymbol{g}|_{\partial\mathcal{P}} = \boldsymbol{N}(-2\tau_g^2 - B_\perp^2) + \boldsymbol{n}(k_n k_g - \nabla_\perp K_M - \nabla_s\tau_g)\,. \tag{B.15}$$

References

[1] B. Alberts, A. Johnson, J. Lewis, D. Morgan, M. Raff, K. Roberts, P. Walter, Molecular Biology of the Cell: Sixth International Student Edition, 500 Tips, Garland Science, Taylor and Francis Group, 2014, https://books.google.com/books?id=1ZUDoQEACAAJ.
[2] J.B. de la Serna, G.J. Schutz, C. Eggeling, M. Cebecauer, There is no simple model of the plasma membrane, Front. Cell Dev. Biol. 4 (1) (2016) 106.
[3] T. Harayama, H. Riezman, Understanding the diversity of membrane lipid composition, Nat. Rev. Mol. Cell Biol. 19 (5) (2018) 281.
[4] S.A. Jewell, Living systems and liquid crystals, Liq. Cryst. 38 (2011) 1699–1714.
[5] U. Seifert, Configurations of fluid membranes and vesicles, Adv. Phys. 46 (1) (1997) 13–137.
[6] S.L. Veatch, S.L. Keller, Separation of liquid phases in giant vesicles of ternary mixtures of phospholipids and cholesterol, Biophys. J. 85 (5) (2003) 3074–3083.
[7] T. Baumgart, B.R. Capraro, C. Zhu, S.L. Das, Thermodynamics and mechanics of membrane curvature generation and sensing by proteins and lipids, Annu. Rev. Phys. Chem. 62 (2011) 483–506.
[8] T. Noyhouzer, C. L'Homme, I. Beaulieu, S. Mazurkiewicz, S. Kuss, H.-B. Kraatz, S. Canesi, J. Mauzeroll, Ferrocene-modified phospholipid: an innovative precursor for redox-triggered drug delivery vesicles selective to cancer cells, Langmuir 32 (17) (2016) 4169–4178.
[9] A. Guckenberger, M.P. Schraml, P.G. Chen, M. Leonetti, S. Gekle, On the bending algorithms for soft objects in flows, Comput. Phys. Commun. 207 (2016) 1–23.
[10] G.J. Doherty, H.T. McMahon, Mechanisms of endocytosis, Annu. Rev. Biochem. 78 (2009) 857–902.
[11] D. Mudhakir, H. Harashima, Learning from the viral journey: how to enter cells and overcome intracellular barriers to reach the nucleus, AAPS J. 11 (2009) 65.
[12] E.N. Hoen, T. Cremer, R. Gallo, L.B. Margols, Extracellular vesicles and viruses: are they close relatives?, Proc. Natl. Acad. Sci. USA 113 (2016) 9155–9161.
[13] V. Budnik, C. Ruiz-Canada, F. Wendler, Extracellular vesicles round off communication in the nervous system, Nat. Rev. Neurosci. 17 (2016) 160–172.
[14] D. Lingwood, K. Simons, Lipid rafts as a membrane-organizing principle, Science 327 (5961) (2010) 46–50.
[15] T. Zhang, C.W. Wolgemuth, Sixth-order accurate schemes for reinitialization and extrapolation in the level set framework, J. Sci. Comput. 83 (2) (2020).
[16] N. Kucerka, M.-P. Nieh, J. Katsaras, Fluid phase lipid areas and bilayer thicknesses of commonly used phosphatidylcholines as a function of temperature, Biochim. Biophys. Acta, Biomembr. 1808 (2011) 2761–2771.
[17] H. Stein, S. Spindler, N. Bonakdar, C. Wang, V. Sandoghdar, Production of isolated giant unilamellar vesicles under high salt concentrations, Front. Physiol. 8 (2017) 63.

[18] J. Happel, H. Brenner, Low Reynolds number hydrodynamics: with special application to particulate media, in: Mechanics of Fluids and Transport Processes, Springer, 1983.
[19] C. Pozrikidis, Fluid Dynamics: Theory, Computation, and Numerical Simulation, Springer, New York, NY, 2017.
[20] L.D. Landau, E.M. Lifshitz, Theory of Elasticity, vol. 7, 3rd ed., Course of Theoretical Physics, Butterworth-Heinemann, Oxford, 1986.
[21] W. Helfrich, Elastic properties of lipid bilayers: theory and possible experiments, Z. Naturforsch., C 28 (11–12) (1973) 693–703.
[22] M. Deserno, Fluid lipid membranes: from differential geometry to curvature stresses, Chem. Phys. Lipids 185 (2015) 11–45.
[23] D.P. Siegel, Fourth-order curvature energy model for the stability of bicontinuous inverted cubic phases in amphiphile- water systems, Langmuir 26 (11) (2010) 8673–8683.
[24] R. Morris, T. Dafforn, M. Turner, Solvated membrane nanodiscoids: a probe for the effects of Gaussian curvature, arXiv preprint, arXiv:1904.00710, 2019.
[25] T. Baumgart, S. Das, W.W. Webb, J.T. Jenkins, Membrane elasticity in giant vesicles with fluid phase coexistence, Biophys. J. 89 (2) (2005) 1067–1080.
[26] G.P. Pomorski, A.K. Menon, Lipid somersaults: uncovering the mechanisms of protein-mediated lipid flipping, Prog. Lipid Res. 64 (2016) 69–84.
[27] L. Miao, U. Seifert, M. Wortis, H.-G. Döbereiner, Budding transitions of fluid-bilayer vesicles: the effect of area-difference elasticity, Phys. Rev. E 49 (6) (1994) 5389.
[28] Q. Du, C. Liu, X. Wang, Simulating the deformation of vesicle membranes under elastic bending energy in three dimensions, J. Comput. Phys. 212 (2) (2006) 757–777.
[29] P. Grinfeld, Introduction to Tensor Analysis and the Calculus of Moving Surfaces, Springer, 2013.
[30] Z.-C. Ou-Yang, W. Helfrich, Bending energy of vesicle membranes: general expressions for the first, second, and third variation of the shape energy and applications to spheres and cylinders, Phys. Rev. A 39 (10) (1989) 5280.
[31] R. Capovilla, J. Guven, Stresses in lipid membranes, J. Phys. A, Math. Gen. 35 (30) (2002) 6233.
[32] R. Capovilla, J. Guven, J. Santiago, Lipid membranes with an edge, Phys. Rev. E 66 (2) (2002) 021607.
[33] Z. Tu, Z. Ou-Yang, Lipid membranes with free edges, Phys. Rev. E 68 (6) (2003) 061915.
[34] D.S. Rodrigues, R.F. Ausas, F. Mut, G.C. Buscaglia, A semi-implicit finite element method for viscous lipid membranes, J. Comput. Phys. 298 (2015) 565–584.
[35] S. Osher, R. Fedkiw, Level Set Methods and Dynamic Implicit Surfaces, vol. 153, Springer Science & Business Media, 2006.
[36] Q. Du, C. Liu, X. Wang, A phase field approach in the numerical study of the elastic bending energy for vesicle membranes, J. Comput. Phys. 198 (2) (2004) 450–468.
[37] S. Osher, J. Sethian, Fronts propagating with curvature-dependent speed: algorithms based on Hamilton-Jacobi formulations, J. Comput. Phys. 79 (1988) 12–49.
[38] J. Lowengrub, J. Allard, S. Aland, Numerical simulation of endocytosis: viscous flow driven by membranes with non-uniformly distributed curvature-inducing molecules, J. Comput. Phys. 309 (2016) 112–128.
[39] P. Smereka, Semi-implicit level set methods for curvature and surface diffusion motion, J. Sci. Comput. 19 (1) (2003) 439–456.
[40] H.-K. Zhao, T. Chan, B. Merriman, S. Osher, A variational level set approach to multiphase motion, J. Comput. Phys. 127 (1) (1996) 179–195.
[41] J.D. Towers, Discretizing delta functions via finite differences and gradient normalization, J. Comput. Phys. 228 (10) (2009) 3816–3836.
[42] X. Wang, Q. Du, Modelling and simulations of multi-component lipid membranes and open membranes via diffuse interface approaches, J. Math. Biol. 56 (3) (2008) 347–371.
[43] C. Li, C. Xu, C. Gui, M.D. Fox, Level set evolution without re-initialization: a new variational formulation, in: 2005 IEEE Computer Society Conference on Computer Vision and Pattern Recognition, CVPR'05, vol. 1, IEEE, 2005, pp. 430–436.
[44] C. Li, C. Xu, C. Gui, M.D. Fox, Distance regularized level set evolution and its application to image segmentation, IEEE Trans. Image Process. 19 (12) (2010) 3243–3254.
[45] S. Aland, S. Egerer, J. Lowengrub, A. Voigt, Diffuse interface models of locally inextensible vesicles in a viscous fluid, J. Comput. Phys. 277 (2014) 32–47.
[46] A.-K. Tornberg, B. Engquist, Numerical approximations of singular source terms in differential equations, J. Comput. Phys. 200 (2) (2004) 462–488.
[47] B. Engquist, A.-K. Tornberg, R. Tsai, Discretization of Dirac delta functions in level set methods, J. Comput. Phys. 207 (1) (2005) 28–51.
[48] P. Smereka, The numerical approximation of a delta function with application to level set methods, J. Comput. Phys. 211 (1) (2006) 77–90.
[49] J.D. Towers, Two methods for discretizing a delta function supported on a level set, J. Comput. Phys. 220 (2) (2007) 915–931.
[50] J.D. Towers, A convergence rate theorem for finite difference approximations to delta functions, J. Comput. Phys. 227 (13) (2008) 6591–6597.
[51] J.D. Towers, Finite difference methods for approximating Heaviside functions, J. Comput. Phys. 228 (9) (2009) 3478–3489.
[52] P. Burchard, L.-T. Cheng, B. Merriman, S. Osher, Motion of curves in three spatial dimensions using a level set approach, J. Comput. Phys. 170 (2) (2001) 720–741.
[53] M. Yanagisawa, M. Imai, T. Taniguchi, Shape deformation of ternary vesicles coupled with phase separation, Phys. Rev. Lett. 100 (14) (2008) 148102.
[54] A. Sakashita, N. Urakami, P. Ziherl, M. Imai, Three-dimensional analysis of lipid vesicle transformations, Soft Matter 8 (2012) 8569–8581.
[55] P. Ziherl, S. Svetina, Nonaxisymmetric phospholipid vesicles: rackets, boomerangs, and starfish, Europhys. Lett. 70 (2005) 690–696.
[56] O.G. Mouritsen, Life-as a Matter of Fat, Springer, 2005.
[57] F. Jülicher, R. Lipowsky, Shape transformations of vesicles with intramembrane domains, Phys. Rev. E 53 (3) (1996) 2670.
[58] T. Taniguchi, Shape deformation and phase separation dynamics of two-component vesicles, Phys. Rev. Lett. 76 (23) (1996) 4444.
[59] J.S. Lowengrub, A. Rätz, A. Voigt, Phase-field modeling of the dynamics of multicomponent vesicles: spinodal decomposition, coarsening, budding, and fission, Phys. Rev. E 79 (3) (2009) 031926.
[60] J.S. Sohn, Y.-H. Tseng, S. Li, A. Voigt, J.S. Lowengrub, Dynamics of multicomponent vesicles in a viscous fluid, J. Comput. Phys. 229 (1) (2010) 119–144.
[61] J. Rossman, X. Jing, G. Leser, R. Lamb, Influenza virus M2 protein mediates ESCRT-independent membrane scission, Cell 142 (2010) 902–913.
[62] J. Armstrong, M. Stevens, Strategic design of extracellular vesicle drug delivery systems, Adv. Drug Deliv. Rev. 130 (2018) 12–16.